Electronic Theses and Dissertations   Theses, Dissertations, and Major Papers

5-11-2018

CMUT Crosstalk Reduction Using Crosslinked Silica Aerogel

Varshitha Yashvanth
University of Windsor

Follow this and additional works at: https://scholar.uwindsor.ca/etd

CMUT Crosstalk Reduction Using Crosslinked Silica Aerogel

By

Varshitha Yashvanth

A Thesis
Submitted to the Faculty of Graduate Studies
through the Department of Electrical and Computer Engineering
in Partial Fulfillment of the Requirements for
the Degree of Master of Applied Science
at the University of Windsor

Windsor, Ontario, Canada

2018

CMUT Crosstalk Reduction Using Crosslinked Silica Aerogel

By

Varshitha Yashvanth

APPROVED BY:

_____

A. Edrisy
Department of Mechanical, Automotive and Materials Engineering

_____

R. Muscedere
Department of Electrical and Computer Engineering

_____

S. Chowdhury, Advisor
Department of Electrical and Computer Engineering

May 3, 2018

DECLARATION OF ORIGINALITY

I hereby certify that I am the sole author of this thesis and that no part of this thesis has been published or submitted for publication.

I certify that, to the best of my knowledge, my thesis does not infringe upon anyone's copyright nor violate any proprietary rights and that any ideas, techniques, quotations, or any other material from the work of other people included in my thesis, published or otherwise, are fully acknowledged in accordance with the standard referencing practices. Furthermore, to the extent that I have included copyrighted material that surpasses the bounds of fair dealing within the meaning of the Canada Copyright Act, I certify that I have obtained a written permission from the copyright owner(s) to include such material(s) in my thesis and have included copies of such copyright clearances to my appendix.

I declare that this is a true copy of my thesis, including any final revisions, as approved by my thesis committee and the Graduate Studies office and that this thesis has not been submitted for a higher degree to any other University or Institution.

ABSTRACT

Inter-element acoustic crosstalk is one of the major concerns which restricts the potential deployment of Capacitive Micromachined Ultrasonic Transducers (CMUTs) in Nondestructive Evaluation (NDE) despite its superior transduction capabilities. This thesis investigates the causes of acoustic crosstalk in CMUTs and develops a novel method of CMUT crosstalk reduction by passivating the CMUT top surface by a thin layer of Di-isocyanate enhanced crosslinked silica aerogel. This powerful technique derives its inspiration from the Scholte waves attenuation techniques as used in boreholes at the permeable formations.

Analytical and 3D finite element analysis in MATLAB and COMSOL Multiphysics, respectively, show that the developed technique can minimize the crosstalk due to Scholte waves at the fluid-solid interfaces by at least 5 dB more at the nearest neighbor as compared to other published techniques. An added advantage of the developed technique is that the level of Scholte wave attenuation can be controlled by altering the porosity of the aerogel layer. A simple and cost-effective fabrication process employing sol-gel and ambient pressure drying processes for the aerogel layer deposition has been developed that doesn't interfere with the basic CMUT operation or fabrication techniques.

DEDICATION

To my parents and sisters

ACKNOWLEDGEMENTS

TABLE OF CONTENTS

LIST OF TABLES

LIST OF FIGURES

LIST OF ABBREVIATIONS

CMUT – Capacitive Micromachined Ultrasonic Transducer

NDE – Nondestructive Evaluation

FEA – Finite Element Analysis

UT – Ultrasonic Testing

PZT – Lead zirconium titanite / Piezoelectric Transducer

CAGR – Compound annual growth rate

MEMS – Microelectromechanical systems

PDMS – Polydimethylsiloxane

BCB – Bisbenzocyclobutene

VLSI – Very large scale integration

CMOS – Complimentary metal oxide semiconductor

HIFU – High intensity focused ultrasound

AC – alternating current

DC – Direct current

FEM – Finite element model

NASA - The National Aeronautics and Space Administration

CNT – Carbon nanotube

RF- resorcinol-formaldehyde

MF – melamine-formaldehyde

SCD – Supercritical Drying

TMOS – Tetramethoxysilane

TEOS - Tetraethoxysilane

Si-OH - silanol group

TMCS – Trimethylchlorosilane

HMDS – Hexamethyldisilazane

Silica-x-aerogel – Crosslinked silica aerogel

FBW- Fractional Bandwidth

RCA – Radio Corporation of America (standard cleaning process)

AP – Adhesion Promoter

RIE – Reactive Ion Etch

UV – Ultra Violet

DI – Di-ionized

APTES – Aminopropyltriethoxysilane

LOR – Lift-off Resist

NOMENCLATURE

f = Centre frequency

c_m = Speed of sound in the medium

ρ_m = Medium density

λ = Wavelength

N = Number of elements

A = Aperture size

D = Element pitch

W = Element width

L = Element length

K = Kerf width

CTL_{avg} = Average crosstalk level

FBW = Fractional bandwidth

Δy = Lateral resolution

Δx = Axial resolution

S = Distance between focus and the CMUT

D_a = Directivity function of the array

θ = off-axis angle

a = Half sidelength

d_m = Diaphragm thickness

d_o = Airgap height

d_i = Insulating layer thickness

t = Top electrode thickness

t_c = Contact pad thickness

L_c = Dielectric post thickness

w_0 = Diaphragm center deflection

σ_0 = Residual stress

ε_0 = Permittivity of free space

V = Bias voltage

P_{Ext} = External pressure

v = Poisson ratio

$f_s(v)$ = Poisson ratio dependent function

D_{eff} = Effective flexural rigidity

E = Young's modulus

C_0 = Parallel plate capacitance

C_{ff} = Fringing field capacitance

C_{Deform} = Capacitance between the deformed diaphragm

T = Tensile force

V_{pi} = Pull-in voltage

Z = Acoustic impedance

c_l = Longitudinal sound velocity

α_l = Longitudinal wave attenuation coefficient

α_t = Transverse wave attenuation coefficient

CHAPTER 1

INTRODUCTION

This chapter presents the objectives of this thesis, explaining the significance of the present work and its outcome. The problem statement is outlined. An overview of state-of-the-art solutions and their limitations are presented, followed by the principal results of the research work. Finally, the thesis outline is listed.

1.1 Goals

According to the latest market research report, the global ultrasonic equipment market for Nondestructive Evaluation (NDE) is expected to reach $3.93 Billion by 2022, at a compound annual growth rate (CAGR) of 8.3% between 2016 and 2022 [1]. Among the test /evaluation equipment, the ultrasonic flaw detectors accounted for a major share of the overall ultrasonic testing market during the forecast period. With the aging infrastructure and the growing need for periodic inspections to monitor the structures, the demand for test equipment with the ability to detect flaws with a high degree of accuracy and reliability without causing damage to the structures or components is the driving force for this tremendous market growth [1].

Most of the commercially available ultrasonic transducers used in ultrasonic test equipment today are piezoelectric. Such transducers rely on the contraction and expansion of a piezoelectric crystal for generation and reception of ultrasound. The emerging capacitive micromachined ultrasonic transducer (CMUT) technology

has the potential to offer many benefits over the traditional piezoelectric transducers as summarized in Table 1.1 [2]. Although a lot of research has been focused towards CMUTs for medical imaging applications, the use of CMUTs for NDE [3] has not yet been extensively explored. This is demanding because ultrasonic NDE can also take advantage of these wide bandwidth MEMS transducers. As technologies advance and the requirement of ultrasonic NDE become more demanding, CMUTs fabricated using micromachining techniques will allow realizing high performance wider fractional bandwidth ultrasonic arrays with higher image resolution.

Table 1-1. Comparison between piezoelectric ultrasonic transducers and CMUTs.

Parameter	Piezoelectric Transducer	CMUT
Fabrication method	Ceramic technology	MEMS technology
Array fabrication	Difficult and high cost, very difficult for 2D array, ring array	Easy and low cost, arrays with through-wafer interconnects
Frequency range	Relatively narrow	Broad
Bandwidth	Moderate, matching layers required	Wide
Array uniformity	Moderate	High
Thermal stability	Low	High
IC integration	No	Yes
Output Pressure	High	Relatively low but improving

While employing ultrasonic testing for solids, a couplant is used to ensure better coupling of the sound waves through the medium on to the test material with

limited attenuation. The most commonly used couplant for material NDE is water. CMUTs when used in immersion have very large bandwidth which can lead to improved resolution [3]. Investigation into the state-of-the-art in CMUT technology suggests that there is a scope for improvement in the CMUT inter-element mechanical cross coupling which is relatively higher than their piezoelectric counterparts due to lack of isolation cuts between the elements.

In this thesis work, a 7.5 MHz linear CMUT array with 64 elements is designed with a thin lossy layer of highly porous, low Young's modulus silica aerogel for a possible application in fluid coupled inspection of pipelines using NDE methods. The novelty of the proposed design is that it exploits the sound speed modulating property of silica aerogel for the first time to minimize the acoustic crosstalk between neighboring elements in a conventional immersion CMUT array while preserving the transducer's performance.

The specific research goals of this research work are:

1. Develop a MEMS based ultrasonic transducer array suitable for NDE using CMUT technology. The developed array would be a highly miniaturized system with reduced crosstalk, improved frequency response, wider bandwidth and higher sensitivity while facilitating easy integration with microelectronic drive and control circuitry.
2. Investigate and validate the CMUT operation for the designed behavior through finite element analysis and analytical models.

3. Study the various cross-coupling mechanisms of acoustic energy among the CMUT cells and arrays by accurate 3D modeling using COMSOL Multiphysics design tools to identify the methods of mitigation of such cross-coupled acoustic energy to improve the transducer performance.

4. Develop a fabrication technique to manufacture the designed CMUT arrays.

1.2 Background

1.2.1 Problem Statement

CMUTs are usually fabricated as large element arrays, each consisting of thousands of CMUT membranes for ultrasound generation and reception. For fluid coupled applications such as in the water medium, the presence of neighboring CMUTs must be taken into account due to an effect known as acoustic crosstalk . When CMUT diaphragms which are close to one another are excited in the water medium, the output acoustic pressure that propagates from each diaphragm has a considerable forcing effect on the neighboring diaphragms as shown in Figure 1-1. This modifies the deflection characteristic of every CMUT diaphragm in the array, and has a significant effect on the overall transducer's performance, both during the transmit and receive operations [4]. This results in inaccuracies and missed defects during image reconstruction in NDE applications.
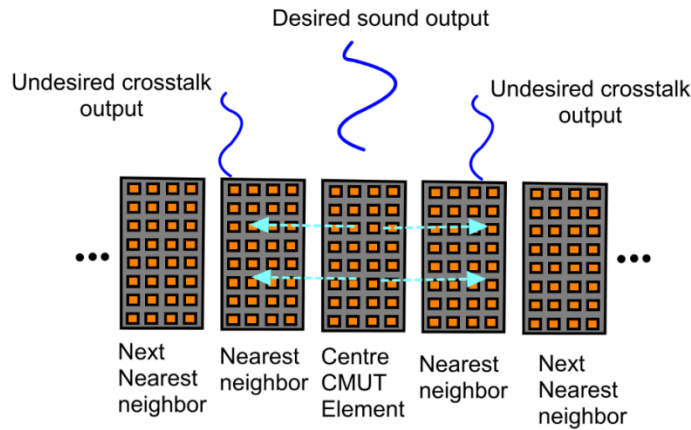
Figure 1-1. Representation of interelement crosstalk.

1.2.2 Notable State-of-the-Art Solutions

In recent years, different approaches have been studied to reduce cross coupling in CMUTs in immersion applications. In [5], a method has been proposed to operate the CMUTs in a pull-in mode that effectively increasing the center frequency as a way to tweak the energy spectrums for crosstalk reduction. Another method of fabricating acoustic bandgaps consisting of an additional passive cavity between the adjacent CMUT elements as shown in Figure 1-2 has been proposed in [6]. This approach resulted in crosstalk reduction of about 10 dB in conventional operation mode (not the pull-in mode) without any detrimental effect on generated acoustic pressure.

Adding a protective sealant layer of PDMS or Parylene on top of the CMUT membranes has been proposed in [7] and [8]. However, the presented experimental results reveal no significant improvement. In another approach as presented in [9], a 150 µm thick PDMS encapsulation layer has been used that showed about -4 dB reduction in crosstalk levels.

5
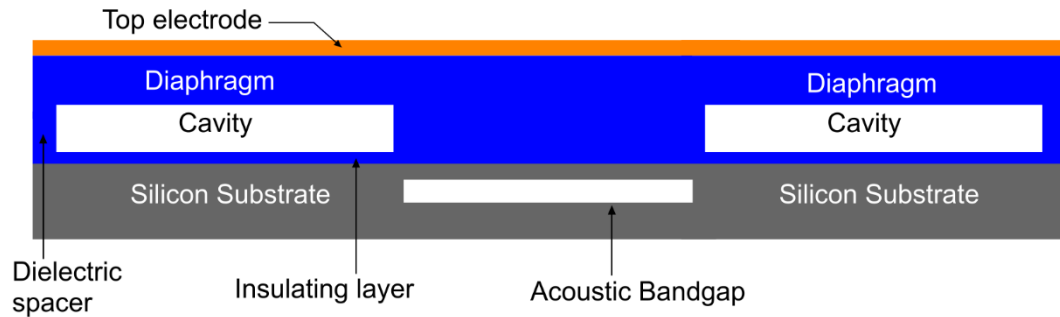
Figure 1-2. CMUT elements with acoustic bandgap between them (the cross-section shows the separation region between the closest cells of neighboring array elements [6]).

Authors in [10] proposed a second periodicity of the CMUT cell spatial configuration to minimize acoustic crosstalk due to substrate reflection. Another numerical study showed a transfer-function-matrix approach to derive modified transmit waveforms on adjacent elements to reduce the acoustic crosstalk [11]. However, this technique relied on programmable waveforms, which introduced circuitry complexity.

1.2.3 Need for Improvement

The aforementioned studies involve the modification of CMUT standard design rule or insist upon additional fabrication steps. Also, some of them call for the CMUT to operate in pull-in mode. It is beneficial to employ a simple crosstalk minimization technique in the conventional mode of operation not involving major design modifications. This thesis work proposes the design of a lossy top passivation layer with optimized thickness to effectively suppress the interface crosstalk wave. Crosslinked silica aerogel is proposed as the passivation layer material to suppress the crosstalk while providing electrical and thermal insulation at the same time. The film vibrates with the diaphragm as a compound laminar plate with very limited attenuation of the transmit/receive energy normal to the

6

transducer surface, preserving the transducer's performance. Simulation results involving CMUT array elements show a crosstalk level reduction of at least 5 dB as compared to [8].

1.3 Contributions

The contributions of this research work are the following:

1. A thin film of highly porous (90%), low Young's modulus (40 MPa) silica aerogel with large surface area (600 N/m^2) is proposed as a solution to reduce CMUT inter-element acoustic crosstalk. A crosstalk level reduction of approximately 5 dB more is observed in the CMUT conventional operation mode. This simple design alteration to the CMUT structure greatly improves the CMUT frequency response while preserving the transducer's static and dynamic performance.

2. To ensure long term durability of the protective layer, silica-x-aerogel which exhibits excellent hydrophobic surface properties and improved mechanical strength has been proposed by introducing di-isocyanates crosslinking agents to enhance the properties of the conventional hydrophilic and delicate silica aerogels. A simple and cost-effective fabrication process employing sol-gel and ambient pressure drying processes for the passivation layer deposition has been developed.

3. A finite element analysis (FEA) with coupled physics to model the CMUT-fluid interaction was performed using COMSOL Multiphysics for a CMUT cell in immersion. The analysis was later extended to large arrays to study the effects of mutual acoustic cross coupling between the array elements.

The model was able to accurately show the peaks and distortions in the frequency response due to acoustic crosstalk.

4. The effect of various design parameters such as CMUT cell sidelength, thickness, sidewall width, diaphragm material, fluid medium and number of cells in an element on the CMUT crosstalk were explored using FEA which served invaluable for understanding the crosstalk patterns and aided further optimizations.

1.4 Thesis Organization

The thesis has been organized in the following manner. Chapter Two begins with a brief introduction to NDE and highlights a few techniques for which ultrasound transducers are generally employed. The transducer specifications for NDE are discussed. An overview of the CMUT technology for NDE is presented and the phenomena of acoustic crosstalk in CMUT arrays is discussed with its causes and side-effects. Finally, the main design specifications of the 7.5 MHz center frequency 64 channel CMUT array for NDE is presented.

Chapter Three presents the mathematical modeling for the CMUT cell. The cell dimensions of the CMUT used in the array are calculated based on the center frequency requirements for the target application. Static and dynamic response of the designed CMUT cell are validated using a cross verification platform comprised of MATLAB based analytical and COMSOL based 3D finite element analysis.

Chapter Four investigates the causes of acoustic crosstalk in CMUT arrays using finite element methods. FEA simulations are performed on several test

CMUT element geometries in varied design scenarios that hold potential for minimizing these undesirable cross-coupling effects.

Chapter Five starts with a brief introduction to the aerogels and explores the feasibility of using silica aerogels as passivation layers on CMUTs for fluid-coupled applications for crosstalk suppression. The crosstalk levels with and without the aerogel layer on the neighboring elements are calculated. Further, the simulated results are compared with the published experimental results of other state-of-the-art PZT and CMUT array designs to evaluate the effectiveness of the designed array.

Chapter Six presents a tentative fabrication process to realize the proposed one-dimensional CMUT linear array. A step by step description of the major process steps involved are presented with the corresponding cross-sectional view.

Conclusions are discussed in Chapter Seven. Chapter Seven also suggests some of the future directions for the research work that include fabrication and experimental characterization of the proposed array and provides final comments on the promising abilities of the aerogels that are yet to be fully exploited.

CHAPTER 2

FLUID COUPLED CMUTs

This chapter highlights the potential of CMUTs for usage in NDE and gives an in-depth review of effects of acoustic inter-element cross-coupling effects in fluid-coupled CMUTs. The key specifications of the designed CMUT array with reduced crosstalk levels for NDE is presented.

2.1 Ultrasonic NDE

Scientist have developed many technologies that take inspiration from nature to solve problems facing mankind. Ultrasound is a perfect example showcasing the trend. Over time, various creative ways to use ultrasound has been explored. Among them, a few common applications include underwater navigation, medical imaging and NDE.

NDE is a group of techniques to inspect material properties and reveal flaws in objects or structures without damaging the unit under test [3] [12]. Common techniques for NDE include ultrasonic, magnetic-particle, eddy current and radiographic. The choice of a suitable technique depends mainly on the type of material, the size of the structure, the type of defect, and the inspection speed [3]. For example, ultrasonic NDE is cost-effective and the most commonly employed technique for weld-joints and inline inspections in pipelines.
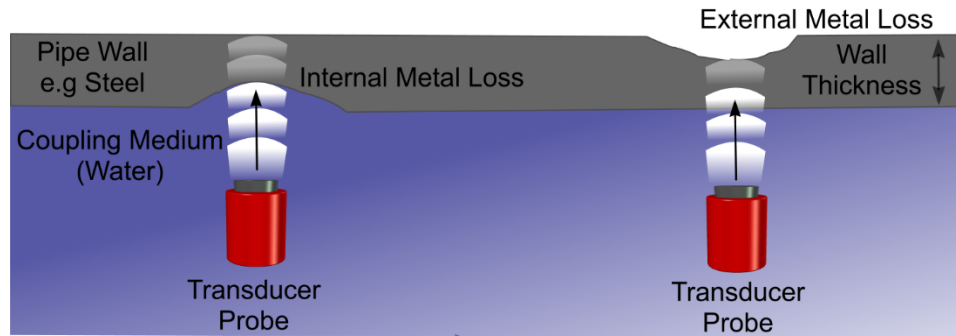
Figure 2-1. Wall thickness measurement using ultrasonic transducers [13] .

Figure 2-1 shows the principle used for pipeline wall thickness measurement. Normal beam testing in pulse-echo mode is used for the detection and measurement of metal loss in pipelines, for instance, corrosion. In such cases, the transducers are aligned perpendicular to the pipe wall that is under inspection. Ultrasound can also be employed for the detection and sizing of cracks in pipelines. Figure 2-2 depicts the crack inspection principle used in NDE. The orientation of the probe depends on the feature of interest. The transducer is aligned so as to direct the acoustic energy into the pipewall at a selected angle as shown in Fig 2-2.
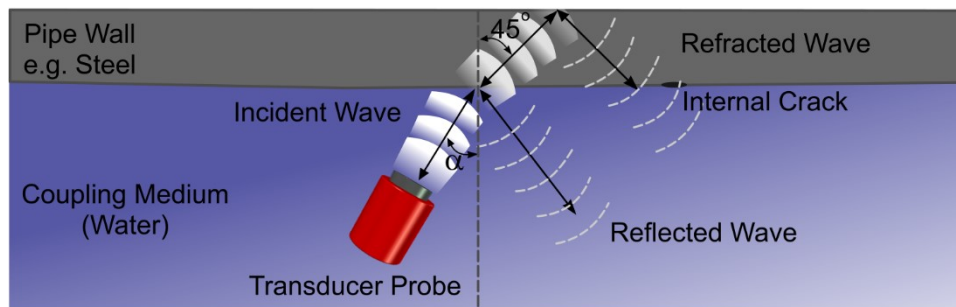
Figure 2-2. Crack detection using ultrasonic transducers [13].

11

2.1.1 Transducer Specifications for NDE

Stainless steel and carbon steel are mainly used in the manufacture of pipelines as they satisfy two main criteria i.e. strength and lost cost. Ultrasound testing is ideally suited for the inspection of pipeline wall thicknesses up to 50 mm.

The transducer center frequency, dynamic range, bandwidth, sensitivity, focal point, pulse repetition frequency etc. have major impact on the detection accuracy, depth and length resolution [13].

The thresholds for depth measurement of metal loss or cracks are set at 1 mm. The reporting accuracy with respect to the depth measurement for the current piezoelectric transducers is approximately ± 0.4 to 0.5 mm. The maximum resolution that can be achieved is about 0.06 mm [13].

2.2 Capacitive Micromachined Ultrasonic Transducers (CMUTs)

The CMUT is a miniaturized ultrasound transmitter and receiver that is fabricated using integrated circuit (IC) technology. It relies on electrostatic principles for ultrasound transmission and reception. The flexural mode of the CMUT diaphragms account for their low mechanical impedance and results in improved energy coupling with the coupling medium. These transducers consume less power, offer excellent electrical and thermal stability, have low noise feature, and are easy to integrate with the underlying CMOS circuitry [2][14][15][16]. Due to these benefits, CMUTs are gradually entering main stream and are considered a potential alternatives to traditional piezoelectric transducers for biomedical

applications, NDE, high intensity focused ultrasound (HIFU), and automotive collision avoidance systems [17][3][18].

2.2.1 CMUT Operation Principle
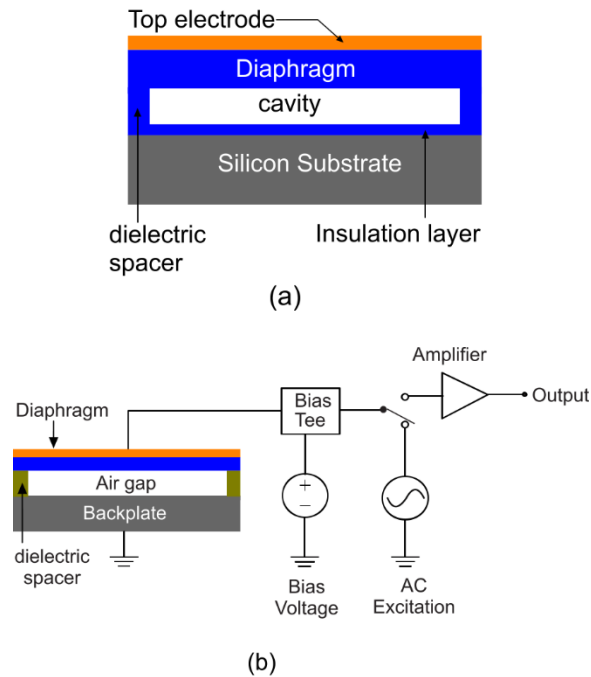
Figure 2-3. (a) Cross section of a CMUT cell (b) Working principle of CMUT.

Figure 2-3(a) shows the cross-sectional schematic view of a CMUT cell. A typical CMUT geometry is built with a square or circular diaphragm separated from a fixed backplate by a small airgap or vacuum allowing the membrane to vibrate. In normal operation, a bias voltage of typically several tens of volts, is applied across the electrodes. The developed electrostatic force pulls the top electrode down and reduces the gap height.

To generate ultrasound, an AC voltage pulse of desired ultrasound frequency is applied across the DC biased CMUT geometry. The resulting time varying electrostatic force of attraction between the diaphragm and the bottom

electrode causes the diaphragm to vibrate at the resonant frequency of the structure, resulting in emission of acoustic waves in the surrounding medium. The same CMUT can also be used to detect ultrasonic waves as shown in Figure 2-3(b). Incoming ultrasound waves cause the top electrode and the diaphragm to deform, producing a change in capacitance between the electrodes [3]. With the bias voltage fixed, a current change corresponding to the incoming acoustic pressure can then be measured with the aid of suitable microelectronic read-out circuitry [19]. Generally, for an ultrasonic transducer, many CMUT cells are connected in parallel to generate enough power. For imaging applications, an array of transducer elements is usually necessary.

2.3   Fluid Coupled CMUTs

As mentioned previously, CMUTs when compared with traditional piezoelectric transducers, are more effective for air-coupled applications. Furthermore, when operated in immersion, CMUTs have a wide bandwidth that could result in an enhanced axial resolution. For ultrasonic testing of solids which requires a coupling medium such as water, immersion coupled CMUTs can provide great benefits.

Investigation into the state-of-the-art in CMUT technology suggests that there is a scope for improvement with respect to dielectric charging [17] and acoustic crosstalk [5] in CMUT arrays. Dielectric charging refers to the trapping of charges within the dielectric layer of a CMUT, causing frequency drift at high bias voltages and affecting the transduction efficiency of the transducer. Acoustic crosstalk means the coupling of energy to neighboring CMUT elements when a

CMUT element is transmitting or receiving, causing unwanted signals to be generated due to the vibration of inactive elements. Significant efforts have been focused towards the reduction of dielectric charging by the usage of a structural material such as BCB (Bisbenzocyclobutene) [17]. In this research work, efforts have been made to investigate the effects of cross coupling in fluid coupled CMUTs and mitigate their effects.

2.3.1 Wave Theory Description of the Problem

Over the years, crosstalk effects have been analyzed extensively using experiments and measurements. It is hypothesized that the acoustic crosstalk is caused by Scholte wave traveling at the fluid-solid interface and also due to the propagating waves in the silicon substrate. In this study, we investigate only the first crosstalk mechanism occurring at the fluid-solid interface. For a better analysis of the surface waves, an understanding of acoustic wavefront propagation at the fluid-solid interface will be very useful [20]. As the wavefront traverses into the solid, it exerts a uniform force around the interface as shown in Figure 2-4. In consequence, compression and shear waves are excited, and body-waves travel in the solid. head-waves are generated in the fluid medium. After the compression and shear waves, the next waves that arrive are the surface waves at the interface. The surface waves that are formed at the interface between solid and liquid are described as Scholte waves.
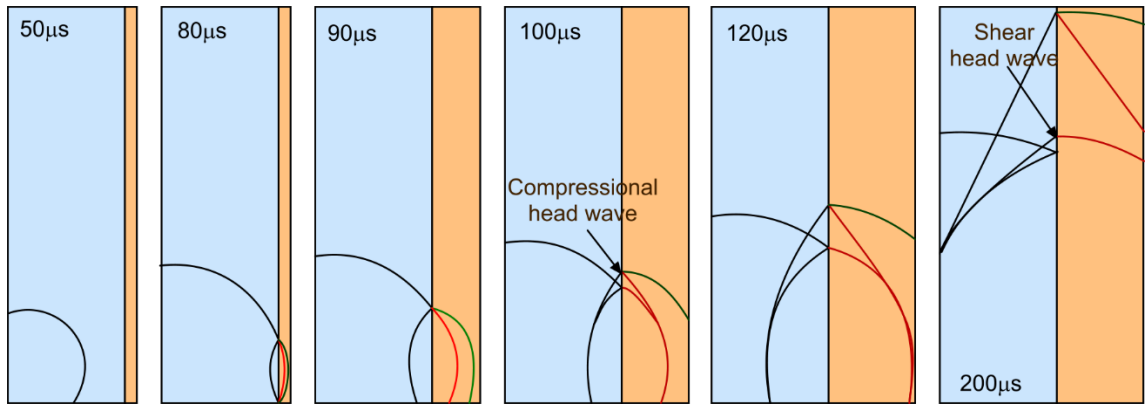
Figure 2-4.Sound wavefront propagation between fluid and a solid. Compressional wave in fluid (black), and in solid(red). Shear waves in solid (green). Reprinted with permission from [20].

The existence of surface waves was first predicted mathematically by Lord Rayleigh in 1885. He calculated the response of an elastic solid in contact with vacuum and found that a wave propagated along the surface whose amplitude decreases with depth [20]. Rayleigh's findings explained the phenomenon of earthquakes as a consequence of waves propagating along the earth's surface. In 1924, Stoneley studied the waves at the interface between two solids and found a similar type of surface wave. The interface wave between a solid and a liquid medium was discovered by Scholte in 1947. However, the terms Stoneley and Scholte waves are used interchangeably to describe the waves at the fluid-solid interface.

The field distribution curve as a function of depth for the Scholte wave at the solid-water interface is as shown in Figure 2-5 [21]. It can be seen that the displacement fields in the solid and the water medium decay rapidly. However, an undamped, non-dispersive wave is observed along the solid-liquid interface that can give rise to significant crosstalk.

16
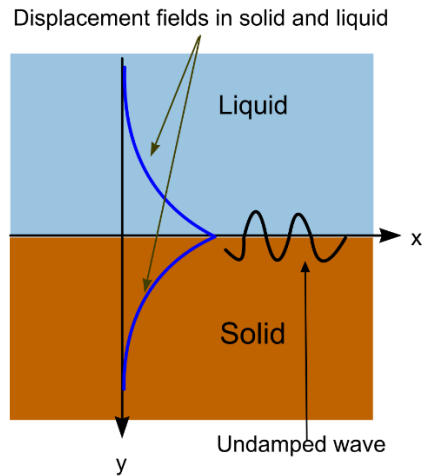
Figure 2-5. Field Distribution curve of Scholte waves. Reprinted with permission from [21]

The velocity dispersion curve as a function of frequency for a 500 µm thick silicon plate loaded with water is plotted in Figure 2-6 [22]. It is seen that the velocity of the wave is nearly non-dispersive after 4 MHz, where it reaches the speed of sound in water. Thus, this large lateral deflection induced at the edge of the vibrating CMUT membrane causes any diaphragm along its acoustic pathway to deflect giving rise to mutual acoustic interactions.

2.3.2 Undesirable Side-effects of Crosstalk

The main objective of transducer arrays used in most ultrasound applications is to radiate acoustic beams with a desired pressure and frequency. At frequencies near the center frequency, crosstalk hinders the uniform deflection of the CMUT diaphragms, leading to variation in amplitude and phase of vibrating diaphragms based on their position in the array. At times, eigen frequencies other than first vibrational mode is also observed. Such a behavior is undesirable as it can alter the sound beam pattern of the individual elements in the array and

17
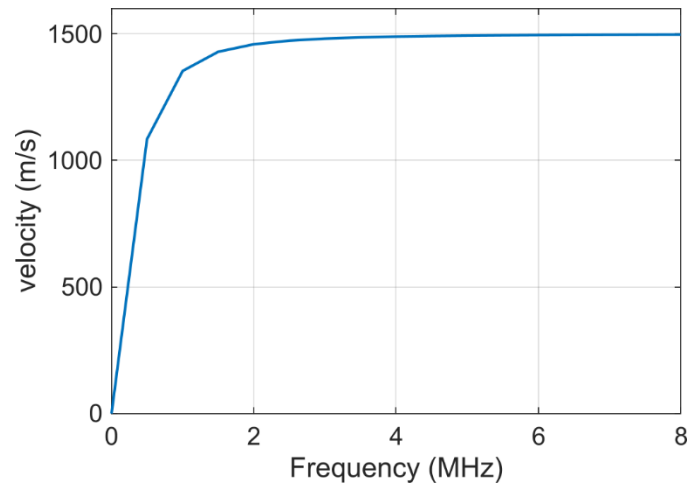
Figure 2-6. Velocity of Scholte waves.

decrease the transducer's capability to accurately resolve features in the surrounding environment [4].

In the receive mode, fluid coupling could cause inactive elements to vibrate. This results in an increase of the effective element aperture and could lead to inaccuracies and missed cracks during image reconstruction [4]. Imaging experiments using CMUTs showed degradation in the axial resolution and bright patterns in the near field due to crosstalk [23].

In all, mutual acoustic interactions bring with them severe effects which manifest themselves in the operational bandwidth of the transducer causing distortions in the frequency response, acoustic power radiation, sound beam patterns and imaging resolutions. Thus, in order to accurately design and optimize CMUT arrays for immersion applications, acoustic crosstalk must be taken into account.

2.4 CMUT Array Design Methodology

For the target NDE application, 7.5 MHz center frequency CMUT with 64-channel has been designed. Each array element is 6 mm long and 100 μm wide. The array elements are comprised of square diaphragms.

Table 2-1. Designed Array Specification.

Symbol	Parameter	Unit	Value
f	Center frequency	MHz	7.5
c_m	Sound speed in the medium	m/s	1500
ρ_m	Medium Density	kg/m^3	1000
λ	Wavelength	μm	200
N	Number of elements		64
A	Aperture size	mm	6.39
D	Element pitch	μm	100
W	Element width (azimuth)	μm	90
L	Element length (elevation)	mm	6
K	Kerf width	μm	10
CTL_{avg}	Average Crosstalk Level	dB	-27
FBW	-6 dB fractional Bandwidth		114%

Each array element consists of 5 cells along the width and the element pitch is maintained to be 100 μm in order to satisfy the Nyquist criteria and avoid grating lobes at large steering angles. Table 2-1 provides the important specifications of the designed array.

2.4.1 Lateral and Axial Resolution

The lateral resolution (Δy) is defined as the minimal distance between two objects on the axis perpendicular to the wave propagation that can be resolved [24]. It depends on the width of the beam and the depth of imaging. The lateral resolution can be expressed as:

$$\Delta y = \left(\frac{1.22\lambda}{A} \right) \times S \qquad\qquad (2.1)$$

where A is the aperture size of the CMUT array and S is the distance between the focus and the CMUT.

The lateral resolution at a particular focus can be maximized by increasing the operating frequency and the aperture size of the CMUT array. The lateral resolution is approximately 162 µm for the designed CMUT.

The axial resolution (Δx) is defined as the minimum distance that can be distinguished between two echo sources in the direction of propagation [25]. The axial resolution can be expressed as:

$$\Delta x = \frac{n\lambda}{2} \qquad\qquad (2.2)$$

where n is the number of scanning pulses, λ is the wavelength and $n\lambda$ is the pulse width.

Decreasing the operating wavelength and reducing the number of scanning pulses can improve the axial resolution of the transducer. For the CMUT designed,

the axial resolution is approximately 0.2 mm when the number of scanning pulses is two.

2.4.2 Axial Pressure Profile

The generated axial pressure profile of the 7.5 MHz CMUT array as a function of distance from the center of the array is shown in Figure 2-7. It is seen that the acoustic pressure close to the array has fluctuations in pressure amplitude in the near field region. Just further from the near field region, the sound pressure is relatively uniform (between 15-20 mm), after which the pressure decreases asymptotically with increasing distance from the array in the far field region.
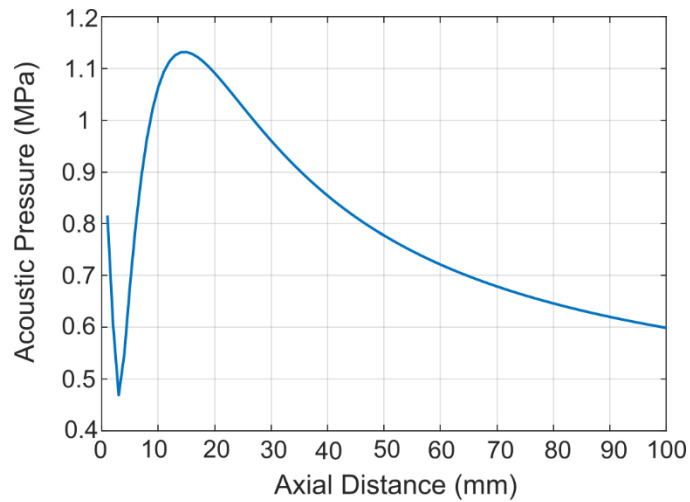
Figure 2-7. Axial pressure profile of 64 element 7.5 MHz CMUT array.

2.4.3 Directivity Pattern

The beam directivity of the CMUT array depends on the transducer aperture size, the operating frequency and the speed of sound in the given medium. It gives the measure of how directional the transmitted sound wave is. The directivity function of the designed CMUT one dimensional linear array with 64 identical elements can be calculated using (2.3) [26].

$$D_a(\theta) = \left| \frac{\sin\left(\frac{\pi W \sin(\theta)}{\lambda}\right)}{\frac{\pi W \sin(\theta)}{\lambda}} \right| \cdot \left| \frac{\sin\left(\frac{\pi W N D \sin(\theta)}{\lambda}\right)}{N \sin\left(\frac{\pi W \sin(\theta)}{\lambda}\right)} \right| \tag{2.3}$$

$$A = N \times W + (N-1) \times K \tag{2.4}$$

where D_a is the directivity function of the array , θ is the off-axis angle (directional angle) , W is the element width, N is the number of elements and D is the element pitch . The directivity pattern of the 64 element CMUT array is simulated in Figure 2-8. It can be seen that the beam pattern of the 64-element array is highly directional and has relatively higher concentrated power in the main lobe than the 16-element array beam.
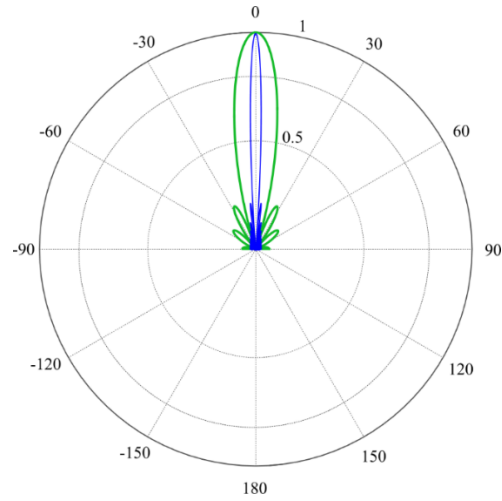
Figure 2-8. Directivity pattern of 16 (green) and 64 (blue) element CMUT array.

Therefore, a highly directional CMUT array with significant acoustic pressure field is designed. The CMUT array geometry, specifically the length and width of the element, are calculated based on the target center frequency of operation.

CHAPTER 3

MODELING OF CMUTs

This chapter presents the analytical and finite element modeling of the CMUT device to calculate some of the primary design parameters. The static and dynamic behavior of the CMUT cells are investigated using COMSOL Multiphysics electro-mechanical simulations.

3.1   Cell Design Methodology

The basic operating principle of the CMUT is that the capacitance between the membrane and the bottom electrode changes dynamically with the incident sound pressure. Thus, the precise calculation of the capacitance between the bottom electrode and the membrane is essential to determine the CMUT transmit and receive sensitivity.

To determine the capacitance change, it is first necessary to calculate the center displacement of the membrane. The diaphragm's center displacement is then used to calculate the deflection profile of the square diaphragm. The capacitance is then obtained by integrating an infinitesimal area of the deformed membrane where the parallel plate approximation holds.

The load-deflection model of a rigidly clamped square diaphragm is used initially to design the approximate behaviour of the CMUT considering geometry and materials. The developed geometry is then modeled using 3-D electromechanical FEA and is later used to study the behaviour of the membrane

24

in the presence of its neighbors in the design space.

3.2 Center Displacement of the Square Diaphragm

The center displacement of the diaphragm gives the maximum capacitance change of the membrane. For this analysis, a homogenous and isotropic diaphragm with fixed edges as shown in Figure 3-1 is assumed.
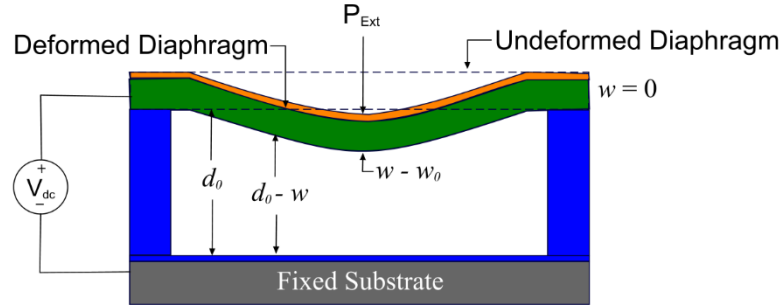
Figure 3-1. CMUT deformation under external pressure

The combined load deflection model of a clamped square multi-layered plate subject to large deflection takes into account the diaphragm stiffness due to nonlinear spring hardening, residual stress, bending, electrostatic spring softening due to the bias voltage, and the external pressure [27] [18]. It is given by:

$$\left[C_s f_s(v) \frac{\tilde{i}}{a^4} \right] w_0 + \left[C_r \frac{\sigma_0 h}{a^2} + C_b \frac{12 D_{eff}}{a^4} - \frac{\varepsilon_0 V^2}{2a} \left(\frac{4a}{d_{eff}^3} + 0.394 \frac{a^{0.25}}{d_{eff}^{2.25}} \right) \right] w_0$$
$$- \left[P_{Ext} + \frac{\varepsilon_0 V^2}{2a} \left(\frac{2a}{d_{eff}^2} + 0.315 \frac{a^{0..25}}{d_{eff}^{1.25}} \right) \right] = 0 \tag{3.1}$$

where w_0 is the diaphragm center deflection, σ_0 is the residual stress, ε_0 is the permittivity of free space, V is the bias voltage, P_{Ext} is the external mechanical

pressure, and v is the Poisson ratio of the diaphragm material. The real root of the equation (3.1) gives the center displacement of the diaphragm.

The values of constants C_r, C_b, and C_s for thin diaphragms are 3.45, 4.06 and 1.9 respectively. The Poisson ratio dependent function $f_s(v)$ in (3.1) is given by [28]:

$$f_s(v) = \frac{1 - 0.271v}{1 - v} \tag{3.2}$$

D_{eff} is the effective flexural rigidity for a multilayered plate:

$$D_{eff} = \frac{AC - B^2}{A} \tag{3.3}$$

where the constants *A, B* and *C* are expressed as:

$$A = \sum_k Q_k (t_k - t_{k-1}), \tag{3.4}$$

$$B = \sum_k Q_k (\frac{t^2_k - t^2_{k-1}}{2}), \tag{3.5}$$

$$C = \sum_k Q_k (\frac{t^3_k - t^3_{k-1}}{3}), \tag{3.6}$$

$$Q_k = \frac{E_k}{1 - v^2_k} \tag{3.7}$$

where E_k is the Young's modulus and v_k is the Poisson's ratio of the kth layer of a laminar plate. The laminar plate constitutes of the top electrode and the diaphragm. In (3.1), the effective Young's modulus $\widetilde{E}$ is the plate modulus and is expressed as:

$$\tilde{E} = \frac{E}{1 - v^2} \tag{3.8}$$

where E is the Young's modulus of the diaphragm material. The effective airgap d_{eff} is defined as:

$$d_{eff} = \frac{d_m}{\varepsilon_{rm}} + \frac{d_t}{\varepsilon_{rt}} + d_o \tag{3.9}$$

where, d_m is the membrane thickness, d_t is top electrode thickness, ε_{rm} is dielectric constant of the membrane, ε_{rt} is dielectric constant of the top electrode and d_o is air gap between diaphragm and backplate.

The deflection profile of a multilayered diaphragm $w(x,y)$ is given by:

$$w(x, y) = \left[w_0 + w_1 \left(\frac{x^2 + y^2}{a^2} \right) + w_2 \left(\frac{x^2 y^2}{a^4} \right) + w_3 \left(\frac{x^4 + y^4}{a^4} \right) \right] \cos^2 \left(\frac{\pi x}{2a} \right) \cos^2 \left(\frac{\pi y}{2a} \right)$$

$$\tag{3.1}$$

Where w_0 is the diaphragm center deflection determined using (3.1)) and the parameters w_1, w_2, and w_3 are determined as:

$$
\begin{aligned}
w_1 &= \frac{0.0013}{\sqrt{t}} w_0, \\
w_2 &= \frac{0.005}{\sqrt{t}} w_0, \\
w_3 &= \frac{0.0021}{\sqrt{t}} w_0
\end{aligned}
\tag{3.21}
$$

The material properties and the specifications of the CMUT cell (Figure 3-2) used in the design are given in Table 3-1 and Table 3-2 respectively. From equations (3.1) and (3.10), the deflection profile of the CMUT membrane at

27
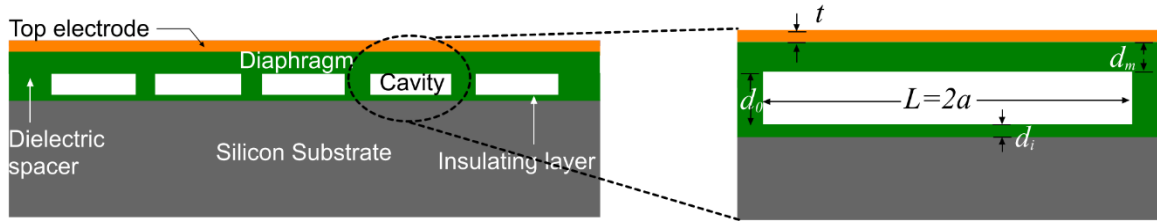
Figure 3-2. Cross-section of a CMUT cell [17].

Table 3-1. Material properties of CMUT cell.

Parameter	Unit	BCB (Diaphragm)	Gold (Top electrode)	Silicon <100> (Substrate)
Density, ρ	kg/m^3	1050	19300	2329
Young's modulus, E	GPa	2.9	70	165
Poisson's ratio, v		0.34	0.44	0.26
Residual stress, σ	MPa	28	106	55
Relative permittivity, ε		2.6	6.9	11.8

Table 3-2. Design specifications of a CMUT cell.

Parameter	Unit	Value
Cell sidelength, $L = 2a$	μm	16
Diaphragm thickness, d_m	μm	1.3
Airgap height, d_o	nm	650
Insulating layer thickness, d_i	nm	100
Top electrode thickness, t	nm	100
Contact pad thickness, t_c	μm	0.4
Dielectric post thickness, L_c	μm	2

28

atmospheric pressure is calculated analytically using MATLAB and is shown in Figure 3-3 (a). The analytical model result is compared with 3D structural analysis is carried out with the solid mechanics interface of COMSOL in Figure 3-3 (b). The parameters like stress, strains and displacements are results of solving Navier - Stoke equation. The center deflection of 5.8 nm is obtained from analytical model which is in good agreement with the FEA center deflection of 5.5 nm with a deviation of about 5.1%.
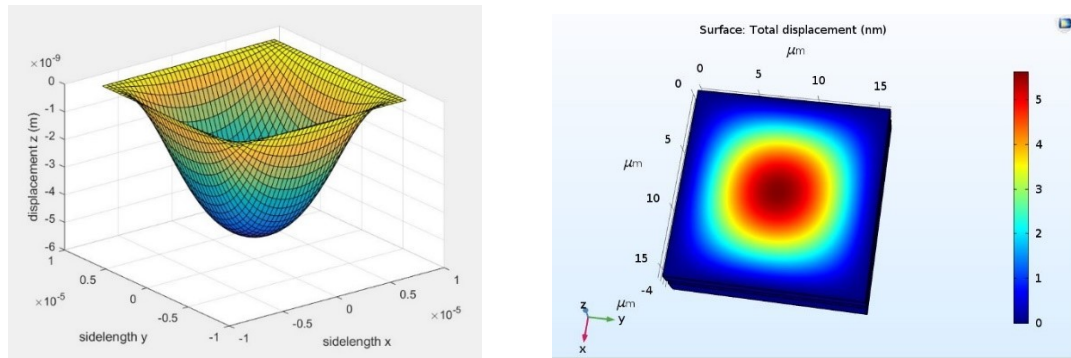
Figure 3-3. Center deflection of the CMUT diaphragm (a) MATLAB analytical Model (b) COMSOL 3D FEA model.

3.3 Capacitance

The total capacitance of an undeformed CMUT membrane can be expressed in terms of a parallel plate capacitor as [27]:

$$C=C_0(1+C_{\text{ff}})$$
(3.3)

where C_0 is the parallel plate capacitance and is given by:

$$C_0 = \frac{\varepsilon_0 4a^2}{d_{\text{eff}}}$$
(3.13)

and C_{ff} is the capacitance due to the fringing fields:

$$C_{ff} = \frac{0.385}{a}\left[d_{eff}\right] + 1.06\left[\frac{1}{2a}\{d_{eff}\}\right]^{0.75} + \frac{0.53}{a}\left[d_c\{d_{eff}\}\right]^{0.5}$$ (3.14)

After deformation, the total capacitance is the sum of the parallel plate capacitance C_{Deform} between the deflecting membrane and the bottom electrode, and the fringing field capacitance C_{ff} and is given by:

$$C = C_{Deform}\left(1 + C_{ff}\right)$$

$$C_{Deform} = \varepsilon_0 \iint_A \frac{dxdy}{d_{eff} - w(x,y)}$$ (3.4)

As the diaphragm sidewalls are fixed, the fringing field capacitance C_{ff} at the fixed edges can be assumed to be unchanged as it is caused mainly by the charges concentrated at the fixed edges.

The capacitance of an undeformed CMUT cell is found to be 1.06 fF in the analytical model. Figure 3-4 shows that plot of capacitance with respect to the DC bias as seen in FEA. The FEA and the analytical model show good agreement with a slight deviation of 6.6%
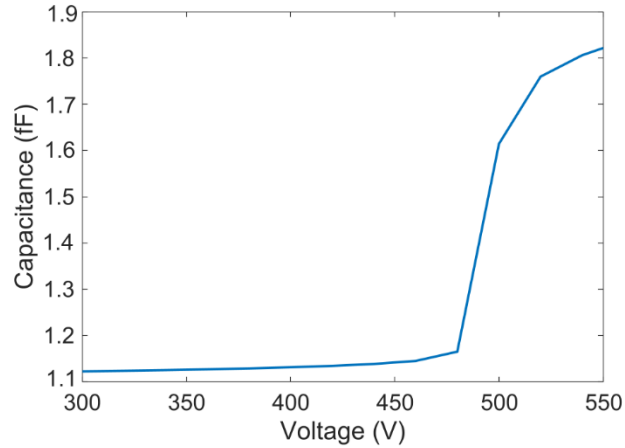
Figure 3-4. Plot of capacitance change as a function of DC bias voltage.

3.4 Resonant Frequency

Resonant frequency in air can be calculated using equation (3.16)

$$f_{res} = \sqrt{\frac{1}{\rho}\left(\frac{D_{eff}\pi^2}{L^4} + \frac{T}{2L^2}\right)} \qquad (3.5)$$

$T = \sigma \times t$ and $L = 2a$, where T is the tensile strength and L is the diaphragm sidelength.

3.5 Pull-in Voltage

The pull-in voltage is a significant design parameter that decides the transmit-receive sensitivity and the dynamic range of the transducer. If the applied DC bias applied to the CMUT is increased beyond a certain value, the electrostatic force of attraction between the top and the bottom electrodes overcomes the restoring spring force of the membrane and the membrane collapses on the bottom electrode which could cause mechanical breakdown of the device. This voltage is called the pull-in voltage. For a given membrane thickness, the pull in voltage can

31

be optimized using the diaphragm's sidelength and the air cavity height. The pull-in voltage for a square diaphragm is given by [27]:

$$V_{pi} = \sqrt{\dfrac{\left(\dfrac{C_r \sigma h}{a^2} + \dfrac{C_b 12 D_{eff}}{a^4}\right) + \left(\dfrac{C_s f_s(v)\tilde{E}h}{a^4}\right)\dfrac{d_{eff}^3}{9}}{3\varepsilon_0 \left(\dfrac{0.665}{d_{eff}^2} + \dfrac{0.2231a^{-0.75}}{d_{eff}^{1.25}}\right)}}$$ (3.6)

(a)   (b)
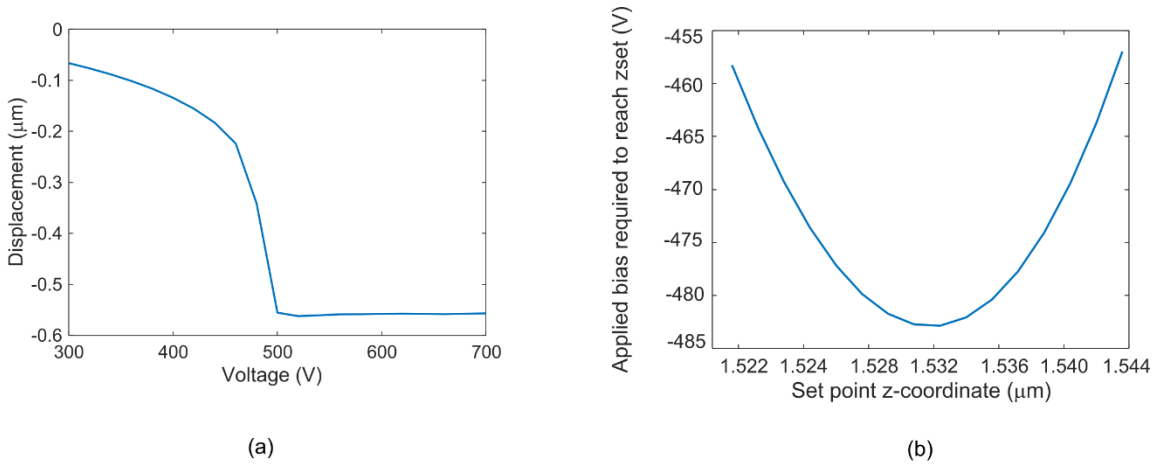
Figure 3-5 (a) and (b). Pull-in voltage of the CMUT diaphragm.

The pull-in voltage of the CMUT cell is calculated to be 452 V using the analytical model. In the FEA, the pull-in occurs at 482 V as shown in Figure 3.5 (a) and (b). The designed FEA accurately predicts the pull-in voltage with a deviation of about 6.1%.

3.6 Dynamic Analysis

Figure 3-6 shows the CMUT cell modelled using the electro-mechanics module in COMSOL. The diaphragm is set to be a linear elastic material and suitable boundary conditions are applied at the edges. Pressure acoustics frequency domain physics module is used for the fluidic medium, and an absorbing layer is

32

used to eliminate the reflection of radiated wave. The maximum element size of meshes is set to be a one-sixth of the smallest wavelength in a frequency domain sweep. The interface between electromechanical and pressure acoustic domains is the fluid–solid coupled boundary, which corresponds to a pressure load on electromechanical domain and a normal acceleration on pressure acoustic domain, respectively. An AC perturbation signal superimposed on a DC voltage are applied to the top electrode.
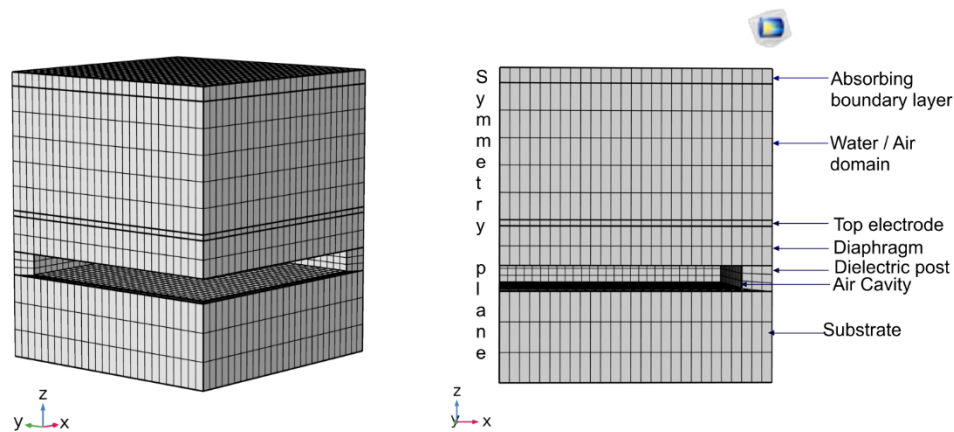
Figure 3-6. CMUT model used in simulation.

The frequency response of the CMUT diaphragm both in air and water medium and shown in Figure 3-7. From the Figure 3-7 (b), it is seen that the maximum displacement 54 nm of the diaphragm in air medium occurs at the designed resonant frequency of 15 MHz whereas the maximum displacement in water medium occurs at 7.5 MHz. The corresponding phase responses are shown in Figures 3-8 (a) and (b).
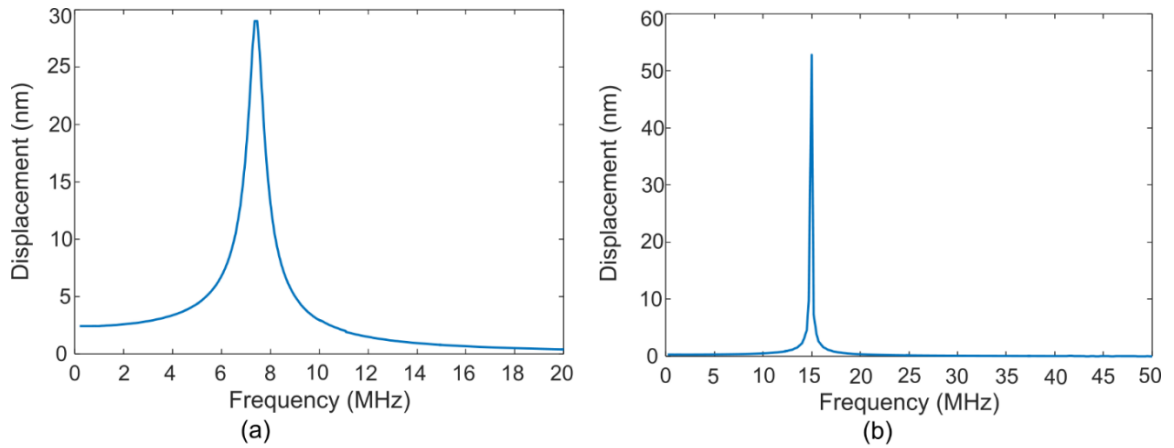
Figure 3-7 Steady state response of the CMUT in (a) water (b) air
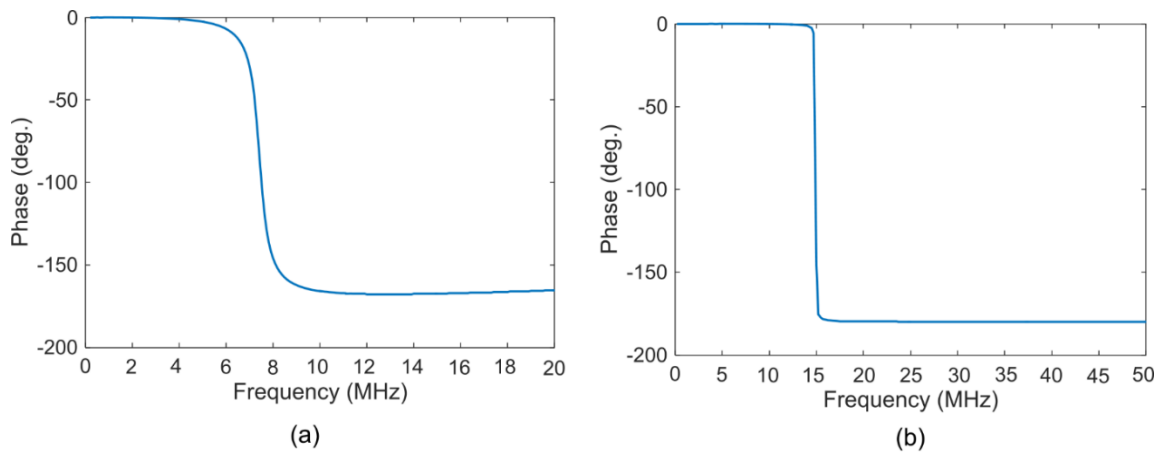
Figure 3-8. Phase Variation with frequency (a) water and (b) air.

Transient response of a CMUT membrane excited with 1 V pulse for 0.1 µs duration, biased at 40 V DC is shown in Figure 3-9.
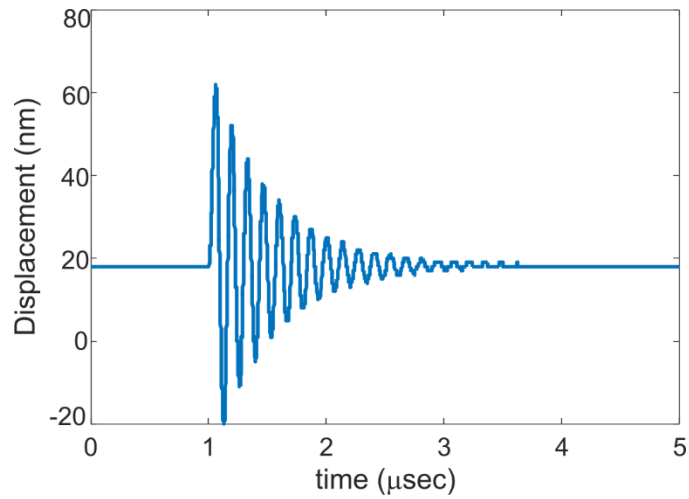
Figure 3-9. Dynamic response of the CMUT cell.

In the preceding studies, the primary design parameters of the CMUT cell are calculated. The static and dynamic performances are analyzed. Further analysis can be directed towards understanding the behavior of CMUT elements and cells in the presence of a neighbor in a fluidic medium.

CHAPTER 4

INVESTIGATION OF ACOUSTIC CROSSTALK IN CMUTs

In this chapter, the fundamental causes of acoustic crosstalk in CMUT arrays are investigated using both analytical and finite element methods. FEA simulations using COMSOL are performed on several hypothetical CMUT elements with a small number of CMUT cells in water medium to investigate the fundamental physics of crosstalk in CMUTs and explore possible ways of crosstalk minimization.

4.1 Potential Contributors for Acoustic Crosstalk in CMUT Cells

Various design parameters such as inter-cell spacing, physical properties of different sidewall materials, acoustic coupling medium and number of cells in the element are investigated to analyze the acoustic cross-coupling among the CMUTs cells and across the elements. Two different test geometries: 1. CMUT Type A and 2. CMUT Type B, with specifications as listed in Table 4-1 are explored in this analysis. The material properties of these two test geometries are listed in Table 4-2.

Table 4-1. Design specifications of CMUT Type A and Type B.

Parameters	Unit	CMUT Type A	CMUT Type B
Membrane Sidelength, $L = 2a$	μm	46	16
Diaphragm thickness, d_m	μm	2.5	1.3
Cavity height, d_o	nm	400	650
Insulator thickness, d_i	nm	100	100
Top electrode Thickness, t	nm	200	100
Resonant frequency in immersion, f	MHz	7.5	7.5

Table 4-2. Material properties of the CMUT Type A and Type B.

Parameter	Unit	BCB (Diaphragm)	Gold (Top electrode)	Silicon <100> (Substrate)
Density, ρ	kg/m³	1050	19300	2329
Young's modulus, E	GPa	2.9	70	165
Poisson's ratio, v		0.34	0.44	0.26
Residual stress, σ	MPa	28	106	55
Relative permittivity, ε		2.6	6.9	11.8

4.1.1 Effects of Inter-cell Spacing in Acoustic Crosstalk in CMUTs

Typically, the CMUT diaphragms are supported by dielectric posts (spacers) that also separate the individual CMUT cells. Increasing the spacer width would increase the inter-cell spacing resulting in a lower fill factor. The effects of this inter-

cell spacing on CMUT crosstalk were studied for the Type A and Type B CMUT test geometries. The cross-section of a 3D FEA simulation model developed in COMSOL acoustic module for this analysis is shown in Figure 4-1.

From Figure 4-2, it can be seen that as the spacing between the cells increases, the irregularities due to the crosstalk in the frequency response diminish and eventually disappear in both types of test geometries.
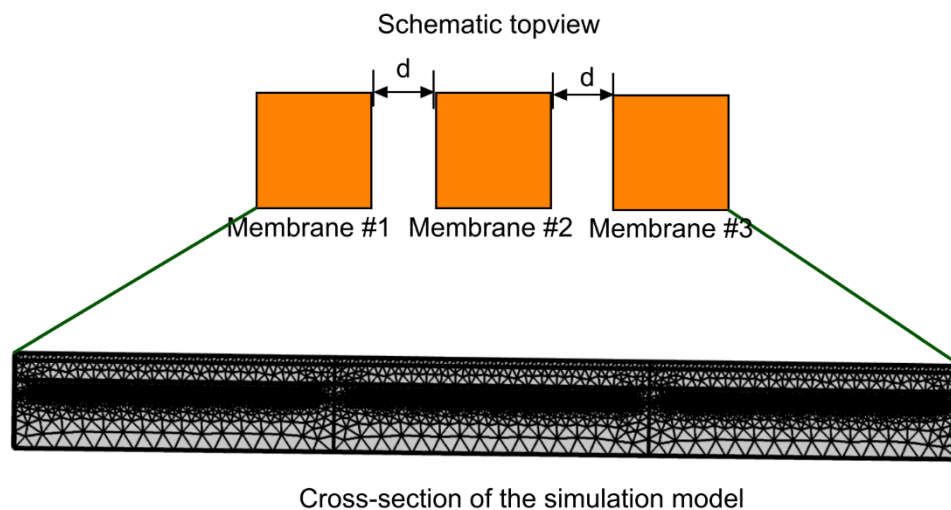
Figure 4-1. 3-cell CMUT element (water medium not shown).

Thus, cross coupling between the cells can be reduced by increasing the spacing between the cells. However, for a fixed sidelength, an increased spacing, decreases the fill factor (active area) of the array and results in a negative impact on the array's acoustic performance. Moreover, a fairly large inter-cell spacing (equal to or greater than twice the cell sidelength) is necessary before any reduction in the cross-coupling effects can be observed. Although this design strategy holds promise, a more detailed investigation on the full array design would be necessary to truly optimize the CMUT array geometry.
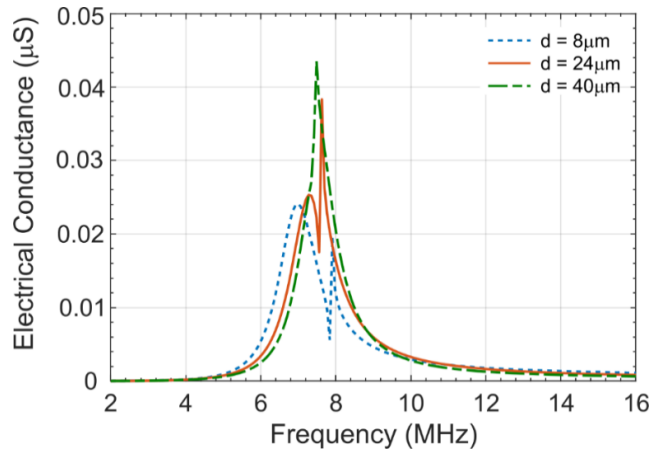
Figure 4-2. Frequency Response with the variation in inter-cell spacing.

4.1.2 Effects of Dielectric Spacer Material on CMUT Crosstalk

The dielectric spacers separating an individual CMUT cell from its neighbors also serve as an efficient pathway for the propagation of the acoustic interface waves to result in crosstalk. An analysis was carried out by switching the spacer material to silicon nitride, silicon dioxide, and BCB (Table 4-3) for the test geometries A and B. Thicknesses of these common spacer materials were varied as well to identify the effects of a respective material's Young's modulus, Poisson's ratio, residual stress, etc. on the amount of crosstalk. From the observations (Figure 4-3), it can be concluded that though the magnitude of the crosstalk varies with the bulk modulus, in general, the amount of crosstalk that manifests as a distorted or split resonance like condition in the frequency response remains unaffected. It is to be noted that as the change of sidewall material (BCB or Silicon nitride) did not make a significant difference to the crosstalk effects, this may be attributed to the high post-cure hardness of BCB of 0.3-0.4 MPa/m$^{1/2}$ which is almost the same as silicon nitride and silicon dioxide. Similar distorted or split resonance effects were observed in the frequency response curves of CMUT Type

A and Type B. Further, the CMUT structural material was also switched to BCB and silicon nitride. Nonetheless, the crosstalk effects persisted.

Table 4-3. Physical Properties of the sidewall material.

Parameter	Unit	BCB	SiO$_2$	Si$_3$N$_4$
Density, ρ	kg/m^3	1050	2170	2500
Young's modulus, E	GPa	2.9	66.3	160
Poisson's ratio, v		0.34	0.15	0.25
Relative permittivity, ε		2.6	3.6	7
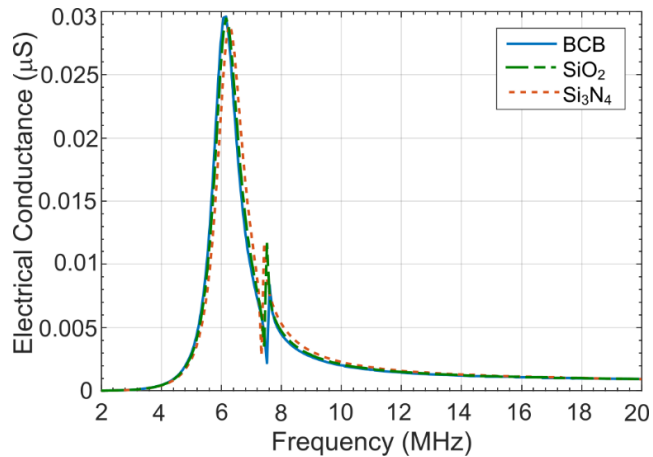
Figure 4-3. Frequency response with different sidewall materials.

4.1.3 Effects of Coupling Medium on Acoustic Crosstalk in CMUTs

The impact of the coupling medium on the crosstalk across the elements of a CMUT array were studied using a 3-cell CMUT configuration as shown in Figure 4-1. Five different coupling media, namely, air, oil, water, glycerin, and sonotrace with physical properties as listed in Table 4-5 has been used in the investigation.

Table 4-4. Physical properties of various ultrasonic testing couplants.

Couplant	Density (kg/m^3)	Sound velocity (m/s)	Acoustic Impedance (MRayl)	Viscosity at 25°C (cP)
Air	1.225	343	0.00042	0.017
Water	1000	1500	1.5	0.89
Oil	900	1420	1.28	450
Glycerin	1280	1920	2.49	620
General purpose couplant (Sonotrace)	1120	1550	1.73	400

The 3 CMUT cell configuration as shown in Figure 4-1 were simulated in COMSOL Multiphysics. When all the three cell membranes were excited simultaneously in a simulated air medium, all the membrane (#1, #2, and #3) exhibit identical deflections and the amount of crosstalk is negligibly small as evident from Figures 4-4(a) and (b). However, when the same simulation was performed in immersion in water, the deflections of the outer membranes (#1 and #3) remained the same whereas the membrane #2 exhibited a different deflection profile as seen in Figure 4-4(b). The response of the cells in oil and glycerin has been seen to be very similar to that of in water. As the medium became denser, membranes showed increased non-uniformity in displacements.
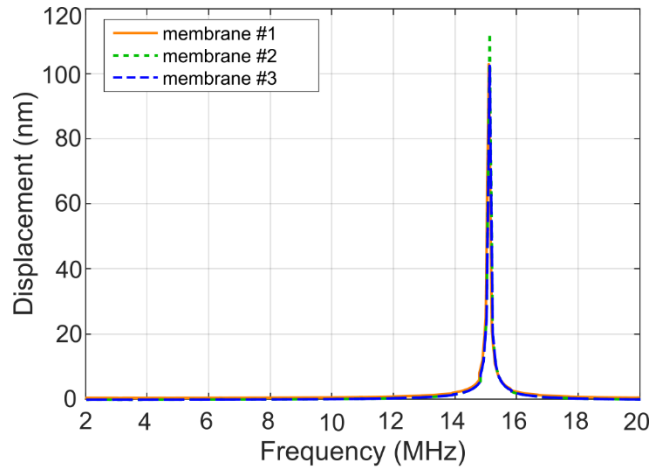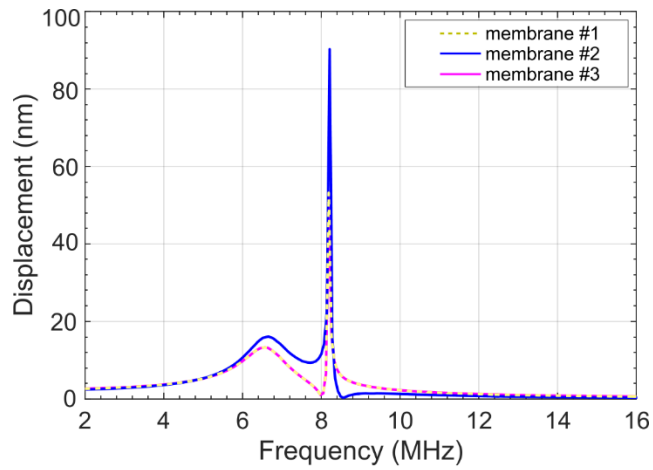
Figure 4-4. Displacement plots of 3-cell configuration in (a) air and (b) water.

In essence, the level of cross coupling among the cells is a function of the density of the fluidic medium. However, as from Table 4-4, cross coupling also depends on the velocity of sound in that medium. And, as the acoustic impedance depends on the sound velocity in the medium ($z = \rho c$), it can be concluded that the crosstalk is strongly dependent on the acoustic impedance of the medium. A lower sound velocity will result in a lower acoustic impedance to minimize crosstalk. However, it is not always feasible to use lower acoustic impedance

medium for ultrasonic evaluation of materials. Consequently, a good strategy to minimize the crosstalk while optimizing the CMUT geometry for a specific target application needs to be explored.

4.1.4 Number of Cells in an Element

In Typical CMUT arrays, individual elements are fabricated to have a number of CMUT cells arranged in a desired pattern to achieve a certain fill factor while satisfying the fabrication constraints and the requirements for array operation. Once the element geometry, specifically length and width, are determined based on the target center frequency of operation, the dimensions and spacing of the CMUT cells can be optimized. In a pre-defined element geometry, smaller CMUT cells require large number of inter-cell spacing that contribute in a lower fill factor (lower active area per element). On the other hand, larger CMUT cells result in smaller number of inter-cell spacing in a pre-specified element geometry to increase the fill factor (higher active area). As the large cells have large diaphragms or membranes, the fluid solid coupling area (active area) is high, that consequently increases the intensity of the Scholte wave. To investigate this phenomenon, 3D FEA simulations were carried out on four CMUT elements with
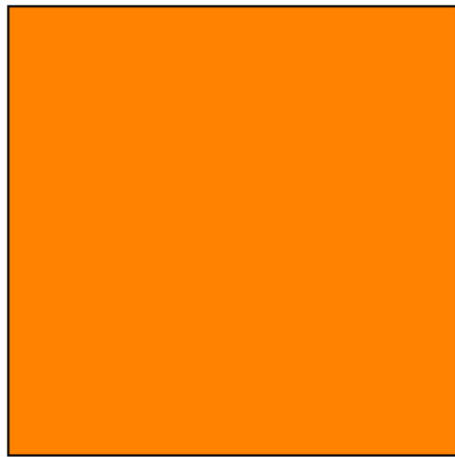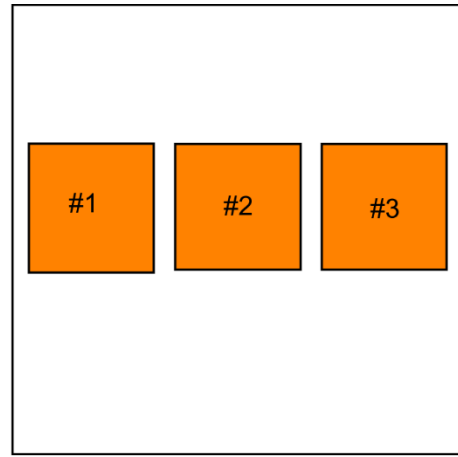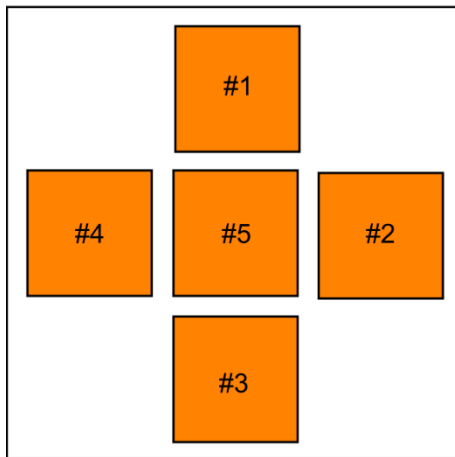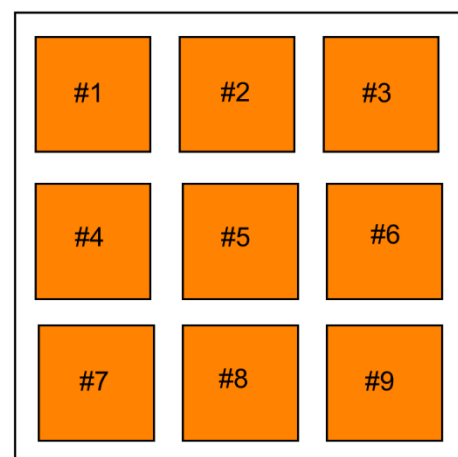
Figure 4-5. Schematic topview of (a) Single cell element (b) 3-cell element (c) 5-cell element (d) 9-cell element.

same lateral dimensions but with different cell configurations as shown in Figures 4-5 (a), (b), (c) and (d). Figure 4-5 (a) shows a single cell element with a large diaphragm whereas Figures 4-5 (b), (c) and (d) show multi cell elements with smaller diaphragms. The frequency response of the single cell element (large diaphragm) and the multi-cell elements are shown in Figures 4-6(a), (b), (c) and

(d) respectively. From Figures 4-6 (a), (b), (c) and (d), it can be seen that as the number of cells per element increases, resonant behavior of the element starts to distort that causes a downshift of the element's resonance peak and introduces uncommon artifacts.
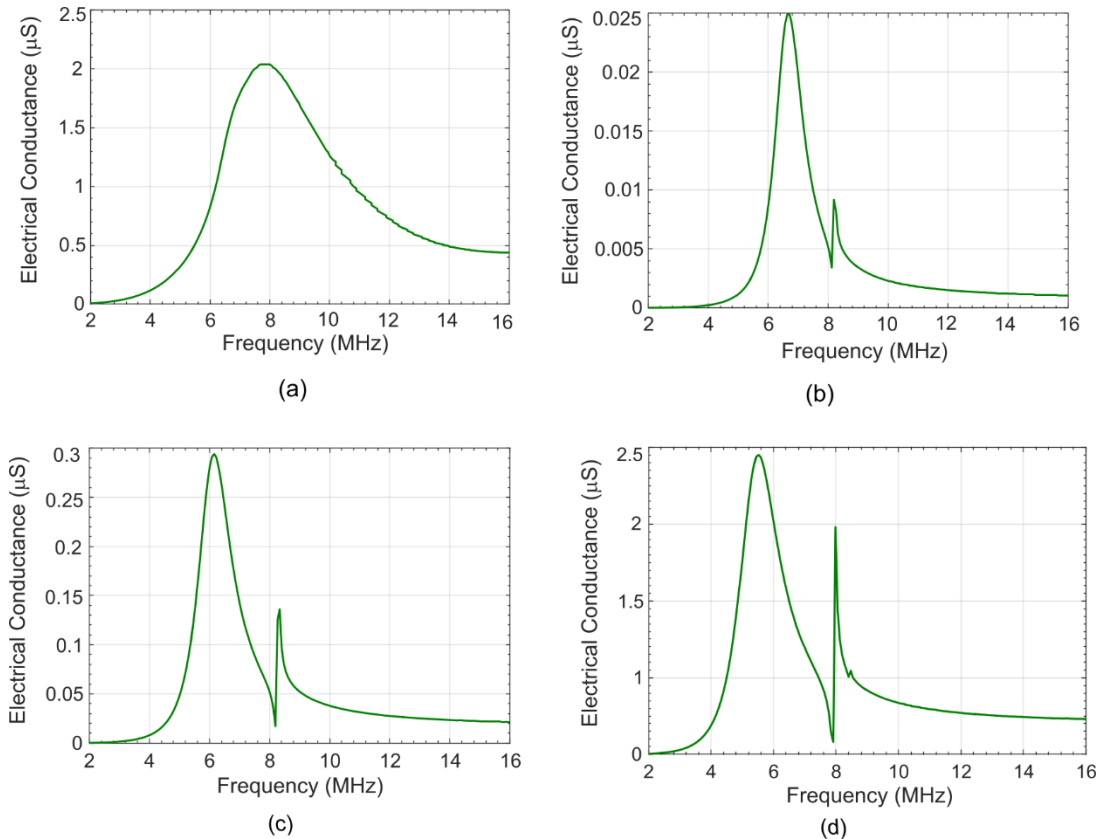
Figure 4-6. Frequency response of (a) Single cell CMUT element (b) 3-cell CMUT element (c) 5-CMUT cell element (d) 9-cell CMUT element.

The cause of such a phenomenon can be understood by examining the deflection plots of 3-cell, 5-cell and 9-cell element shown in Figs. 4-7 and 4-8 and is explained below.

The interface waves which are generated at the fluid-solid interface couple to the adjacent membrane through the dielectric spacers. Although identical dimensions are assumed for the membranes and spacers in an element, the
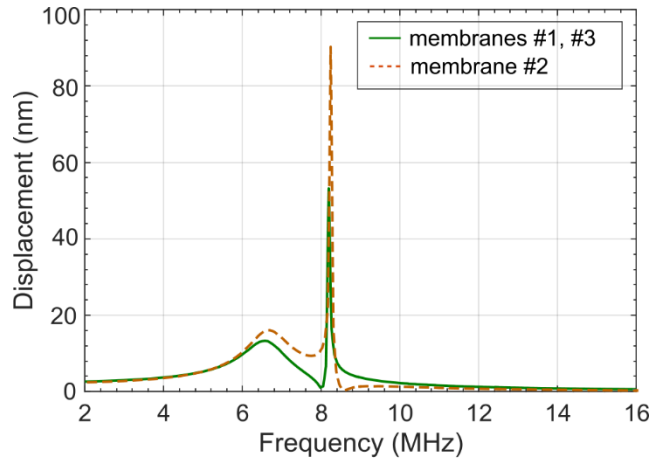
(a)
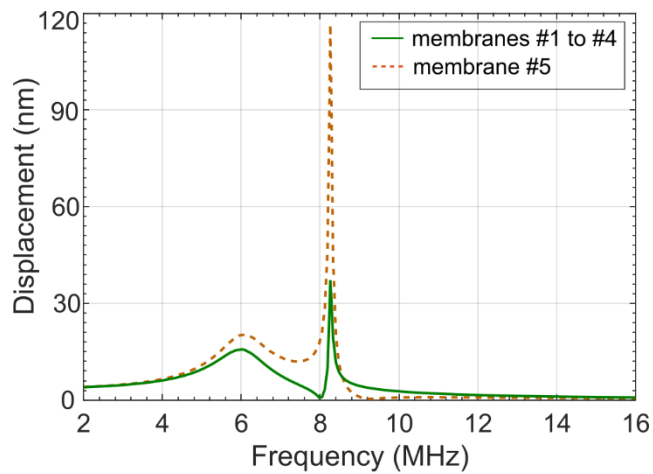
(b)

Figure 4-7. Membrane displacements of (a) 3-cell CMUT element (b) 5-cell CMUT element.

amount of their exposure to Scholte wave intensities depend on the reflection and

propagation of the Scholte waves at the cell boundaries and their respective

phases. Consequently, there is a probability that at a certain location in an element,

the Scholte waves are in phase and undergo constructive interference whereas in

some other locations, the Scholte waves suffer destructive interference when they

are out of phase. This will cause a change of the intensity of the Scholte waves

affecting any particular diaphragm. A CMUT cell at a higher Scholte wave intensity
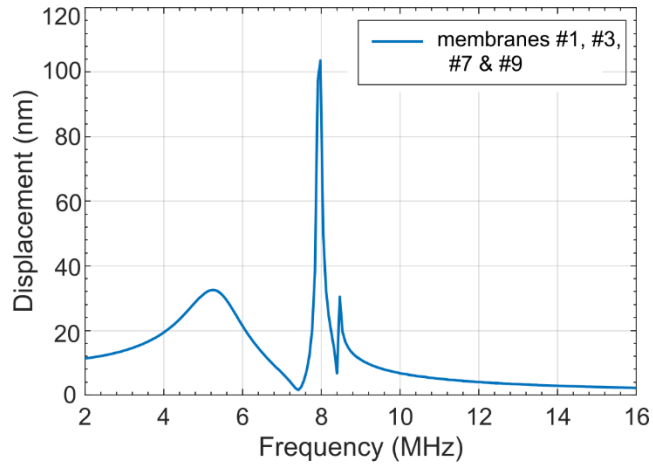
(a)
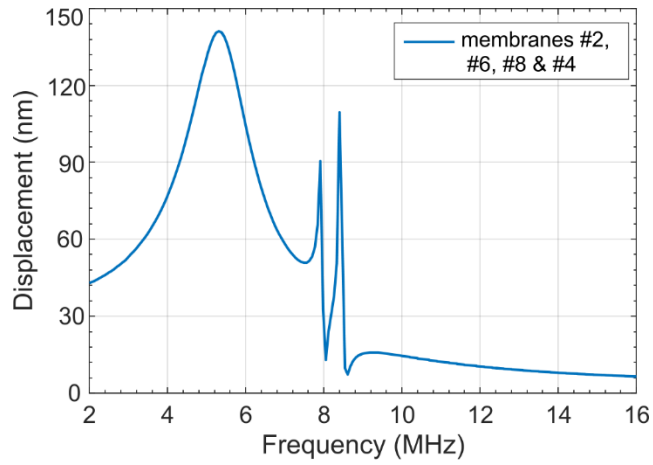
(b)
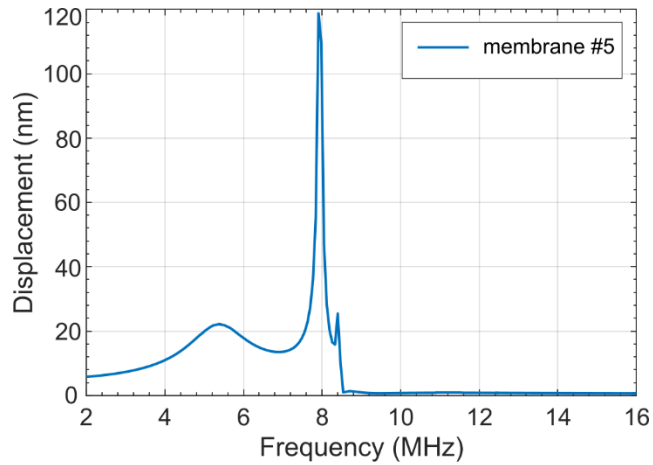
(c)

Figure 4-8.(a), (b) and (c) Membrane displacements of 9-cell CMUT element.

location, will experience the effect more whereas a CMUT cell at a lower Scholte wave intensity location, will experience the effect less. CMUT cells which are at different geometrical locations in an element or array but suffer identical Scholte wave intensities, will have the same frequency response. COMSOL 3D FEA simulation results as shown in Figures 4-7 and 4-8 support this argument.

The displacement plots of the 3-cell element as shown in Figure 4-7(a) shows that membrane #1 and membrane #3 (the outer membranes) show identical deflection curves. However, the middle membrane #2 deflects differently from their counterparts. Similar effects were also observed in higher multi-cell elements (5-cell and 9 cell elements).

Thus, it can be concluded that the interface waves (Scholte waves) generated at the neighboring CMUT cells is a major source of crosstalk in CMUT elements that distorts the frequency response of the element by shifting the resonant frequency and effects the displacement. The higher the number of cells in an element, the more distortion and resonance frequency shift occurs. Another interesting pattern that has been noticed is that the distortion intensity depends on the symmetrical location of the CMUT cells in an element. The centrally symmetric cells (#2, #4, #6, and #8 in a 9 cell CMUT element) show the worst case scenario as compared to the central cell. In essence, crosstalk due to the Scholte waves is a serious issue that can significantly degrade the resonance characteristics of a CMUT and compromise the NDE quality.

4.2   Scientific Approach to Mitigate CMUT Crosstalk

It can be inferred from the foregoing analysis that in a given fluidic medium, the dimensions of a CMUT cell and its position in a CMUT element can have a significant impact on the frequency response of the CMUT array. Consequently, it can affect the accuracy of the target ultrasound based NDE. Increasing the spacing between the membranes decreases the sharpness of the crosstalk peaks but degrades the bandwidth of the devices.

In order to come up with an optimal design with these design parameters, a more focused investigation involving several permutations through the various design parameters such as membrane sidelength, their arrangement within the element, inter-cell spacing, and element pitch would be necessary. Also, care must be taken so that the important CMUT array performance specifications such as acoustic output pressure, sensitivity and bandwidth are not compromised during the process.

Further thought is put into developing a strategy to mitigate the intensity of the Scholte wave that would not involve any major design modifications of the CMUT structures. The study of borehole acoustic waves suggests that the Scholte waves, especially the low frequency ones, are sensitive to formation permeability at the fluid-solid interface as shown in Figure 4-9 [20]. When the waves propagates through permeable formations, the fluid vibrates relative to solid, which attenuates the wave and slows it down. Based on this principle, the possibility of introducing a thin highly porous nano-structural protective layer on top of CMUT surface which

would attenuate the Scholte wave propagation and minimize crosstalk effects is explored.
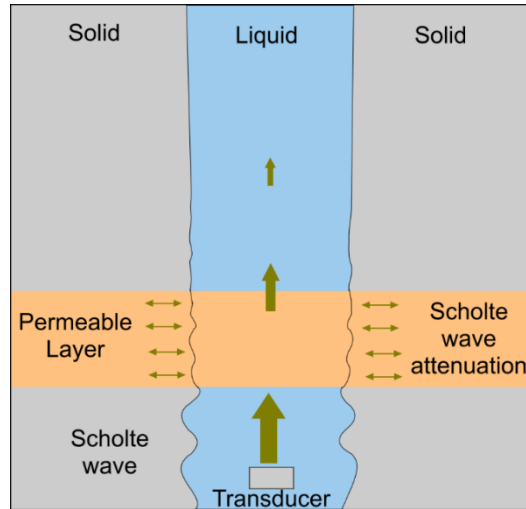
Figure 4-9. Scholte waves propagation through a borehole. Reprinted with permission from [20].

Silica aerogel is a highly porous material with pores sizes in the range of 20nm. They have a very high surface area due to their extremely small particle size. The small granules tend to be compact and have a higher silica content for the same volume resulting in high packing density. The high silica content presents a highly tortuous path for the Scholte waves to propagate through the nano-pores of the silica granules. The wave particles undergo numerous internal reflections within the aerogel's network, bouncing back and forth between the nano pores of the silica framework, and most of the energy is contained close the surface of the gels. It is also an excellent electrical and thermal insulator even with a few micrometer thicknesses which makes it ideal for usage as a passivation layer on the CMUT surface. Additionally, it will not interfere with the CMUT's transduction properties when used as passivation layer on the CMUT, it acts as a laminar thin

film (compound plate) with the top electrode and the diaphragm, while efficiently

deflecting with the top electrode to radiate or receive acoustic energy.

CHAPTER 5

CROSSTALK REDUCTION WITH SILICA AEROGEL PASSIVATION LAYER

This chapter explores the feasibility of using silica aerogel as a passivating layer on CMUTs for fluid-coupled applications for crosstalk suppression. 3D FEA simulations were carried out in COMSOL Multiphysics to calculate the reduction in the level of crosstalk with the aerogel passivation. The simulated results have been validated by comparison with other published results of state-of-the-art CMUT transducer arrays.

5.1   Aerogels

Aerogels are low-density, highly porous (~98%) solid networks of a gel that are commonly fabricated using sol-gel chemistry [31][32]. These mesoporous (2-50 nm pores) interconnected nanostructures filled with air exhibit many dramatically enhanced material properties over their non-aerogel counterparts of the same substance (for instance, very large surface area) with reduced mechanical strength [33].

Due to their several unique properties, aerogels are garnering interest from both academic and industrial sectors. Numerous commercial applications of the polymer aerogels are found such as in architectural field [34] and thermal insulation [35], as catalysts [36], filters, and nanoparticle detectors [37].

5.1.1 Comparative Study of Different Types of Aerogels

Following [38], aerogels can be broadly classified into organic and inorganic types based on their composition. Among the aerogels, silica aerogel is the most widely used due to its extraordinary properties such as high specific surface area (500–1200 m^2/g), high porosity (80–99.8%), low density (~0.003 g/cm^3), low thermal conductivity (0.01$Wm^{-1}K^{-1}$), low dielectric constant (k= 1.0–2.0), low speed of sound (100-500m/s) and low refractive index (~1.05) [32][39]. These unique properties make them extremely favorable for a wide variety of industrial applications.

Metal Oxide aerogels are colorful electrically conductive aerogels which act as catalysts for chemical transformations [39]. They are also employed in the manufacture of explosives.

In [38], it has also been mentioned that a metal chalcogenide is a compound made from a metal and a chalcogenide element such as sulfur, selenium, and tellurium. Most common metal chalcogenide aerogels are cadmium sulfide (CdS), cadmium selenide (CdSe), cadmium telluride (CdTe), zinc sulfide (ZnS), and lead telluride (PbTe) [39]. Metal chalcogenides are slowly gaining popularity as they can be easily transformed into quantum dots which find their application in the advanced LED flat-panel displays. Additionally, they are used as photovoltaic materials (converts sunlight into electrical energy) in affordable solar panels as they can be easily produced at ambient conditions.

Table 5-1. Comparison of different aerogel types [28-39].

	Inorganic Aerogels			Organic Aerogels	
Aerogel Type	Silica (SiO$_2$)	Metal Oxide (M$_x$O$_y$)	Chalcogenide (M$_x$S$_y$, M$_x$Se$_y$, M$_x$Te$_y$)	Carbon (CNT, Graphene)	Polymer (RF, MF)
Density (g/cm^3)	0.0011-0.650	0.03-0.2	0.02-0.1	0.02-0.5	0.02-0.6
Surface Area (m^2/g)	500-1200	150-700	100-600	600-800	350-1025
Avg. Pore Size (nm)	20	5-20	2-20	3-20	3-20
Gel Synthesis	Hydrolysis of silicon alkoxide/ acid-driven condensation of waterglass	Epoxide-assisted gelation of aluminum salts or hydolysis of aluminum tri-sec-butoxide	Oxidative removal of thiolate from preformed nanoparticles	Polymerization of 1,3-dihydroxybenzene with methanal	Polymerization of 1,3-dihydroxybenzene with methanal
Drying Method	Supercritical CO$_2$ or high-temperature drying from organic solvent	Supercritical CO2 or high-temperature drying from organic solvent	Supercritical CO2	Supercritical CO2 followed by pyrolysis at 400°C-1050°C under inert gas	Supercritical CO$_2$
Thermal Conductivity (W/mK)	0.016-0.03	29	110-20	120-320	0.20-0.1
Electrical Conductivity (S/cm)	10^{-18}	1-25	1-20	1-14.7	10^{-6} to 10^{-20}
Acoustic Speed (m/s)	100-800	400-900	400-1000	300-900	300-900
Young's Modulus (MPa)	0.05-400	0.55	0.4-200	0.5-500	0.5-500
Transparency	Clear to foggy	Clear to foggy	opaque	Opaque	Partially translucent to opaque
Application	Mars Rovers Comet dust catchers Windows	Electrodes fuel cells explosives dyes glazes	Chemical sensors Energy Storage applications, Photovoltaic materials	Supercapacitors fuel cells desalination groups	Precursors for CNT NASA Research

Organic Carbon aerogels are extremely high surface area materials and hold great potential for supercapacitors and fuel cells for energy-efficient automobiles [36] [39]. By altering the density, carbon aerogels can be made electrically conductive. Carbon aerogels reflect only a very small percentage of incident radiation and are used as solar energy collectors.

Polymer aerogels such as resorcinol-formaldehyde (RF) and melamine-formaldehyde (MF) [40] aerogels comprise an important class of organic aerogels, and they are studied for their potential uses in thermal insulation and as precursors of electrically conducting carbon aerogels.

Silica aerogel exhibits the lowest speed of sound. Silica aerogel also is a good thermal and electrical insulator and can be deposited using relatively easier and low cost sol-gel deposition techniques. Due to the lowest speed of sound in silica aerogel and its ease of microfabrication, this thesis introduces the use of silica aerogel to mitigate the propagation of Scholte waves at the fluid-solid interface of a CMUT array to minimize acoustic inter-element crosstalk as reviewed in Chapter 4.

5.2   Silica Aerogel

Figure 5-1 shows the structure of a typical silica aerogel, which is highly porous.
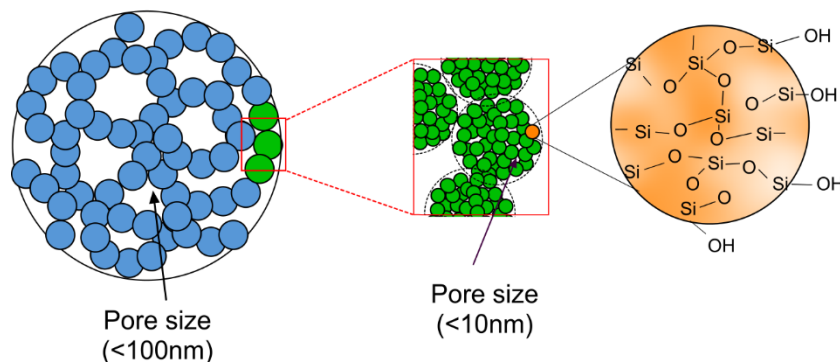
Figure 5-1.Structural network of an aerogel.

The longitudinal acoustic velocity is typically of the order of 100 m/s [31], due to which silica aerogels are suitable for applications requiring acoustic

attenuation. The acoustic propagation in aerogels depends on the interstitial gas nature and pressure [41], the aerogel density, and the texture [42] . The propagation of an acoustic wave is attenuated both in amplitude and velocity because the wave energy is progressively transferred from the gas to the aerogel solid network, over the entire aerogel workpiece thickness [43] [36]. The longitudinal sound velocity also follows a scaling behavior with density (Figure 5-2 (a)) as shown:

$$c_l \propto \rho^{1.3} \tag{5.1}$$

where c_l is the longitudinal velocity. These scaling laws can be explained in terms of percolation theory [44] or due to fractural network structure [45].
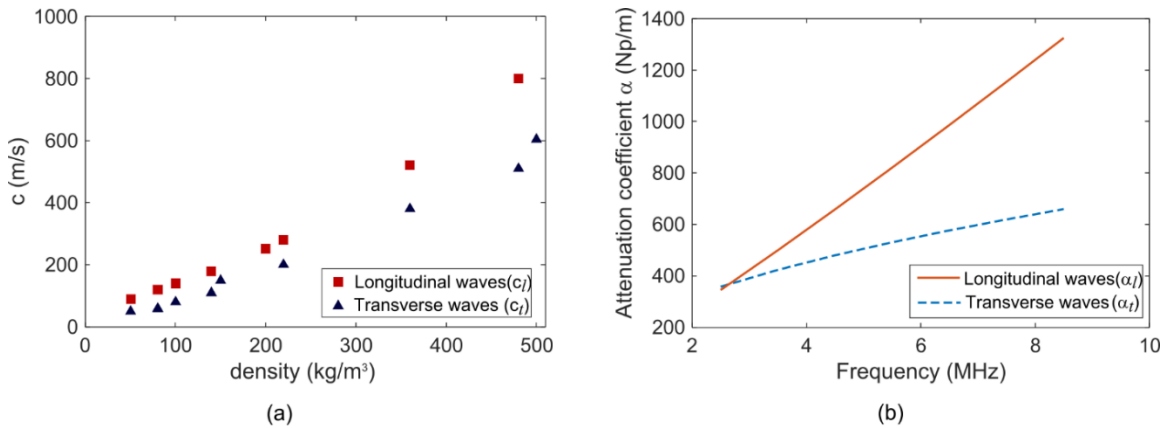
Figure 5-2. (a) Speed of sound in different density aerogel (b) Attenuation coefficient of the sound waves with frequency.

The longitudinal wave attenuation coefficient (α_l) and the transverse wave attenuation coefficient (α_t) follow frequency law as given in [60]

$$\alpha_l(f) = \alpha_{l1} \cdot f \tag{5.2}$$

$$\alpha_t(f) = \alpha_{t1} \cdot f^{0.5 \pm 0.15} \tag{5.3}$$

where $\alpha_{l1} = 1.2 \times 10^{-4} \, Np/(mHz)$ and $\alpha_{t1} = 0.226 \, Np/m/Hz^{0.5}$ .The corresponding curves for frequency range 2.5 MHz to 10 MHz is as shown in Figure 5-2 (b).
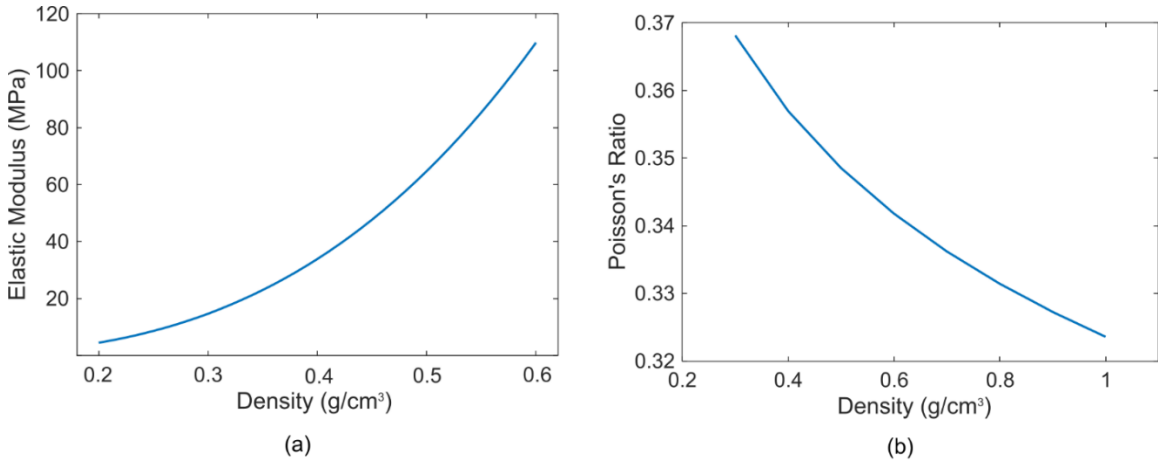
Figure 5-3. (a) Young's Modulus and (b) Poisson's ratio variation with density.

The compressive strength, tensile strength, and elastic modulus of silica aerogels are very low and largely depend on the network connectivity and aerogel density [46]. Assuming bulk silica aerogel to be a homogenous material, the mechanical properties of silica aerogels can be described by the elastic modulus and the Poisson's ratio. The Young's modulus and the Poisson's ratio of these nano-porous aerogels follow a power law relation [47] with density as shown:

$$E \, \alpha \, \rho^{3.11 \pm 0.21} \tag{5.4}$$

$$v = 0.3236 \cdot \rho^{-0.107} \tag{5.5}$$

where E is the Young's modulus, v is the Poisson's ratio and ρ is the density. Corresponding curves for different densities are shown in Figures 5-3 (a) and (b).

57

Also, the shear and rupture moduli display scaling with density. One of the major characteristics of silica aerogels is their very high thermal insulation, typically of the order of $0.015W/m \cdot K$ at ambient temperature [39] and pressure. These values are relatively lower than the thermal conductivity of air under the similar conditions. Thus, silica aerogel is one of the best thermal insulating materials.

5.2.1 Preparation of Silica Aerogel

Silica gels are prepared through the sol-gel chemistry, in which nanoparticles suspended in a liquid solution (i.e., a sol) are invoked to interconnect and form a continuous, porous, nanostructured network of particles across the volume of the liquid medium (i.e., a gel). Two gel preparation techniques: silica alkoxide gelation and waterglass method are discussed in the following section.

5.2.1.1 Silica Alkaoxide Gelation with Supercritical Drying

The most common technique of silica aerogel preparation involves sol preparation using silicon alkoxide precursors (usually either tetramethoxysilane or tetraethoxysilane) followed by supercritical drying (SCD) to form the aerogel [46]. The main sol-gel reactions are as shown in Figure 5-4.

Although the alkoxide gelation and SCD are the standard methods for synthesizing aerogels in industrial settings, the process happens to be very energy intensive and expensive for our use. Recent progress has shown ambient pressure drying using inorganic sodium silicate precursors (waterglass) could be employed to produce low cost silica aerogel with properties very close to those fabricated

using traditional processes [39]. However, the resultant product from waterglass method may sometimes be less porous and might need additional purification steps, it is still very efficient technology for our usage.

R = alkyl group (such as CH_3, C_2H_4)

Hydrolysis

Water Condensation

Alcohol Condensation
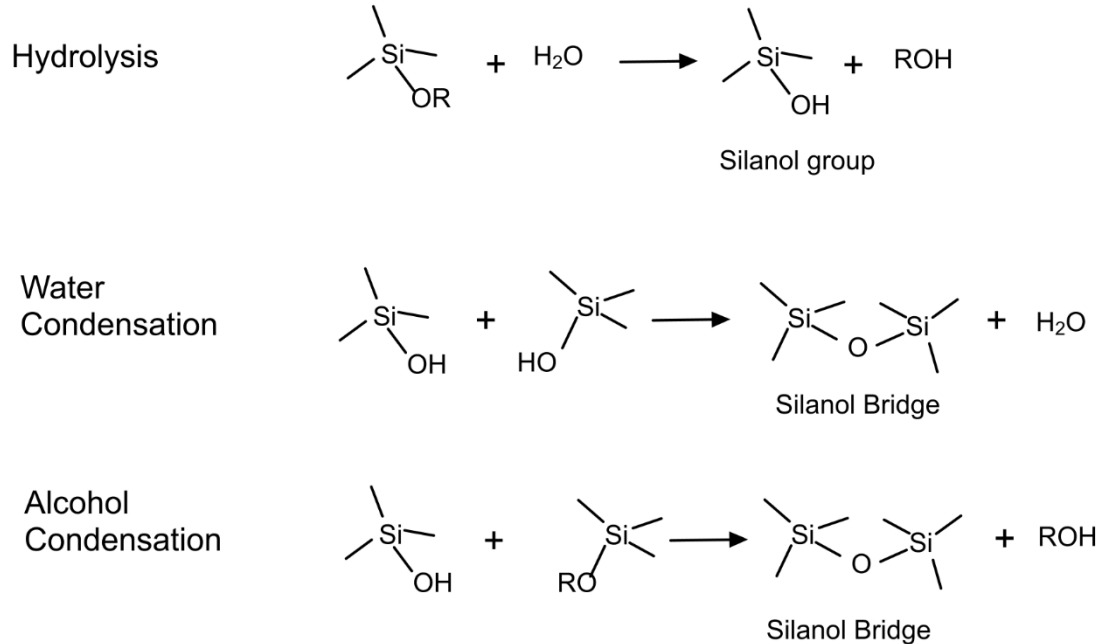
Figure 5-4. Sol-gel reactions with silicon alkoxide.

5.2.1.2 Waterglass Method

In this method, silica gels are synthesized from an aqueous solution of sodium silicate. Sodium silicates are soluble in water, and when dissolved the resulting solution is referred to as waterglass. The gelation of the waterglass solution is initiated by passing the aqueous solution through a column filled with an ion exchange resin where the sodium ions Na+ are replaced by H^+ ions forming silicic acid H_2SiO_3 as shown in Figure 5-5 by adding Lewis base (F-) or Bronsted base (OH-) [54]. Once silanol groups form, the silicate molecules form siloxane bonds

with other silicate molecules and bridge together to form nanoparticles, resulting

in a sol.

Figure 5-5. Waterglass method of sol preparation using ion-exchange resin. Reprinted with permission from [54].

5.2.2 Purifying, Aging and Ambient Drying of Silica Gels

Once a silica gel has been formed, a number of steps involving washing

and solvent exchange is carried out to exchange the pore fluid from water to

alcohol and to diffuse out any impurities. The gel's structural framework is then strengthened during the ageing process.

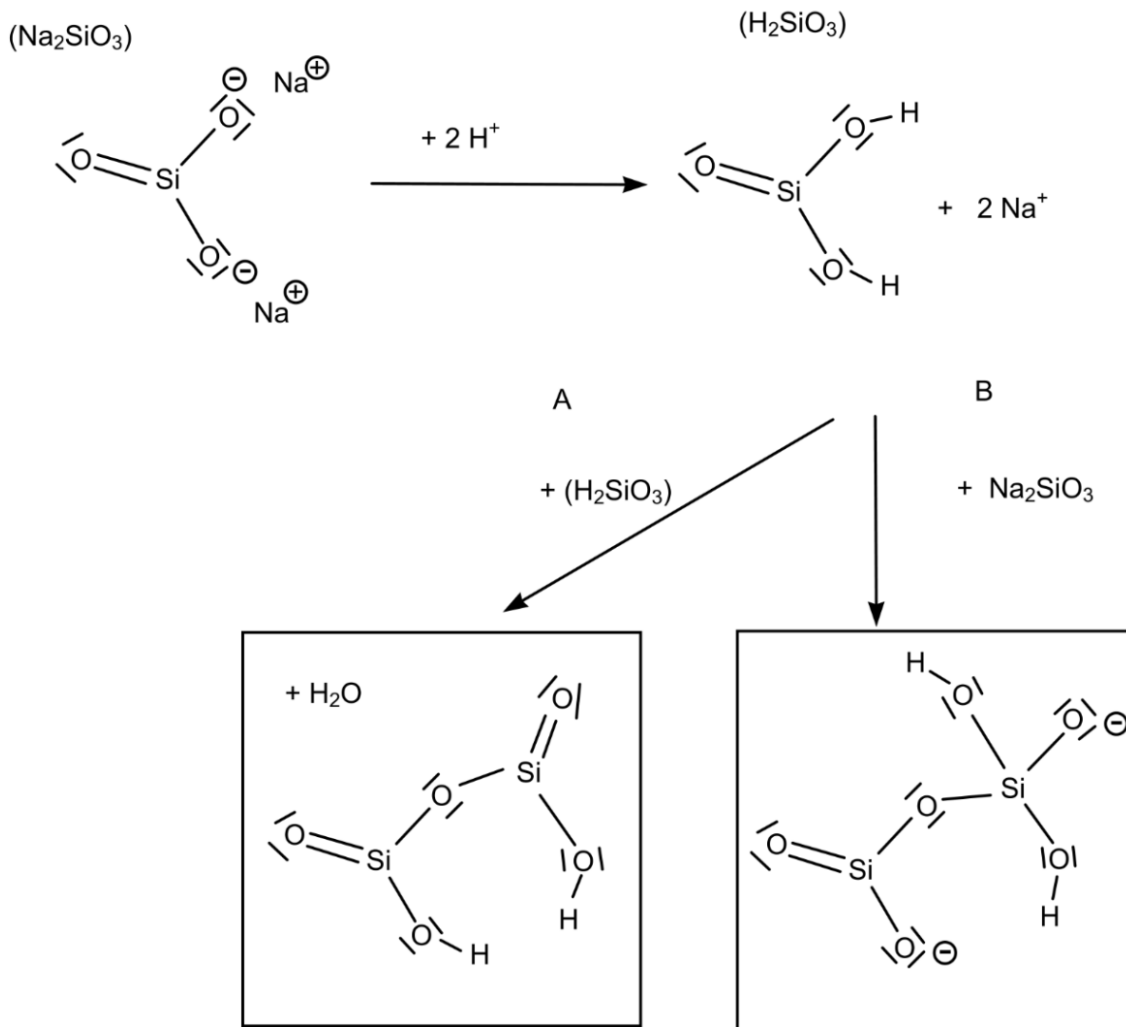It should be noted that conventionally prepared aerogels are hydrophilic in nature as they usually contain a lot of unreacted silanol (Si-OH) groups on their surface. If they are used directly in the ambient drying process, the capillary forces exerted by the environment causes structural collapse of the aerogel (xerogel). Thus, the gel must be modified with hydrophobization agents prior to ambient pressure drying to make the surface hydrophobic.

5.2.3 Hydrophobic Silica Aerogel

The degree of hydrophilicity of the surface can be measured by the contact angle that a droplet makes with a surface. Relation between the surface topology of hydrophobic and hydrophilic surfaces is illustrated in Figure 5-6.

$(\theta<90^{o})$ $(\theta=90^{o}-150^{o})$

θ θ

Hydrophilic Surface   Hydrophobic Surface
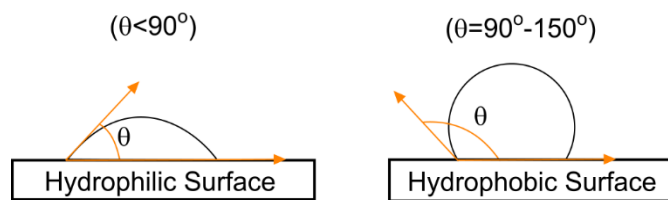
Figure 5-6. Representation of contact angles on hydrophilic and hydrophobic surfaces.

Surface hydrophobization of silanol groups in the silica gels is done by introducing agents such as TMCS (Trimethylchlorosilane) or HMDS (Hexamethyldisilazane) [54] to the gel to react once the impurities such as water and alcohol are completely removed by treating them linear hydrocarbon such as heptane or

pentane so that they are not used up by undesired side reactions. The process reaction is as shown in Figure 5-7.

Hydrophobic surface is an added advantage as the aerogels will no longer be sensitive to moisture content in the environment. The gel can now be dried through ambient drying process (25°C to 50°C)
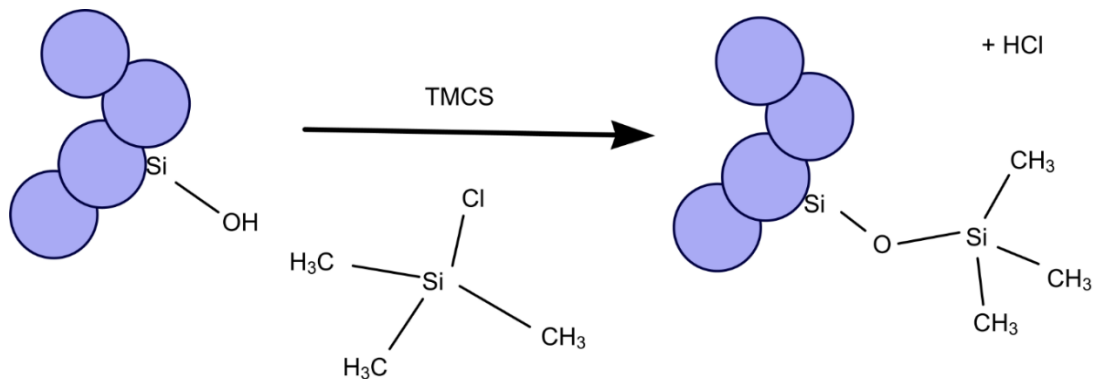
Figure 5-7. Hydrophobization of surface silanol group in silica gel with trimethylchlorosilane (TMCS). Reprinted with permission from [54] .

5.2.4 Crosslinked Aerogels

A typical silica aerogel has a very high compression strength. However, the force has to be applied softly [39]. With the developments in research, the aerogels can now be made strong and flexible while still retaining its hydrophobic properties. The gel used for making silica aerogels is soaked in solutions containing di-isocyanates crosslinking agents. It is then heated so that the di-isocyanates agent starts to react and undergo bonding with the silanol group. The gel is then slowly evaporatively dry. Because of the polymer linking, the end product is a silica

aerogel with increased mechanical strength [39]. It can resist the capillary stress

caused by evaporating that an ordinary gel would not sustain. An added advantage

is that it is hydrophobic and does not require supercritical drying. However, there

is a slight increase in its density.
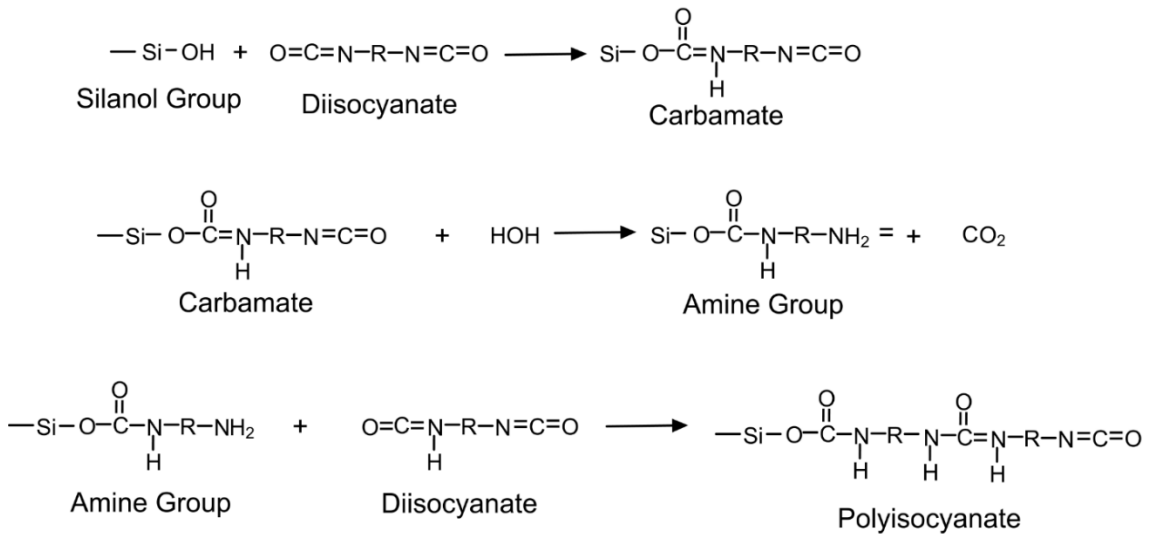
Figure 5-8. Reaction for amine modified aerogel crosslinking with di-isocyanates [39].

5.3 Acoustic Crosstalk Reduction Methodology Using Silica Aerogel

5.3.1 Design Specifications of Silica Aerogel Thin Film Layer

Based on the requirement for a hydrophobic silica aerogel with improved

mechanical strength, silica-x-aerogel is chosen for the target application of CMUT

crosstalk reduction. The physical properties of the aerogel used in simulations are

shown in Table 5-2.)

Table 5-2. Design Specifications of silica aerogel thin film layer.

Parameter	Value	Value
Density, ρ	g/cm^3	0.4
Young's Modulus, E	MPa	50
Poisson's ratio, v		0.34
Speed of sound, c	m/s	300

5.3.2 Static Behavior Analysis

The displacement versus the DC bias voltage of a CMUT with the specifications (as shown in Table 5-3 and 5-4) is plotted in Figure 5-9 with a 2-μm thick aerogel coating on the top of the diaphragm metal layer to verify the prediction of static operating point. The pull-in voltage of the aerogel coated CMUT was found to be 482 V which is equal to the pull-in voltage of the CMUT without the aerogel coating as seen in Figure 5-9. This indicates that the aerogel coating is significantly less stiff than the diaphragm at DC bias and does not affect the pull-in voltage.
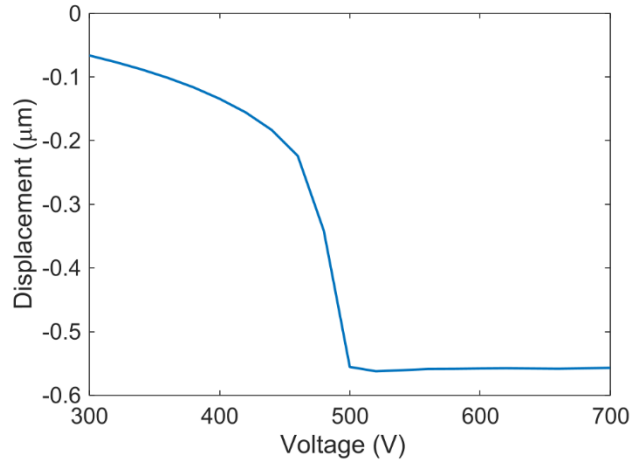
Figure 5-9. The pull-in voltage of the device with aerogel.

5.3.3 Aerogel Passivation Layer Thickness Determination

The investigation was initially started with an arbitrary thickness of aerogel layer. Once it was found that silica aerogel had the potential to minimize crosstalk effects in CMUT arrays, different analyses were carried out to optimize the thickness of the aerogel protection layer to provide the sufficient acoustic suppression for the target application.

The aerogel coating thickness as a function of frequency is plotted for sound velocity 1500 m/s in water. Figure 5-10 indicates the coating thickness for various
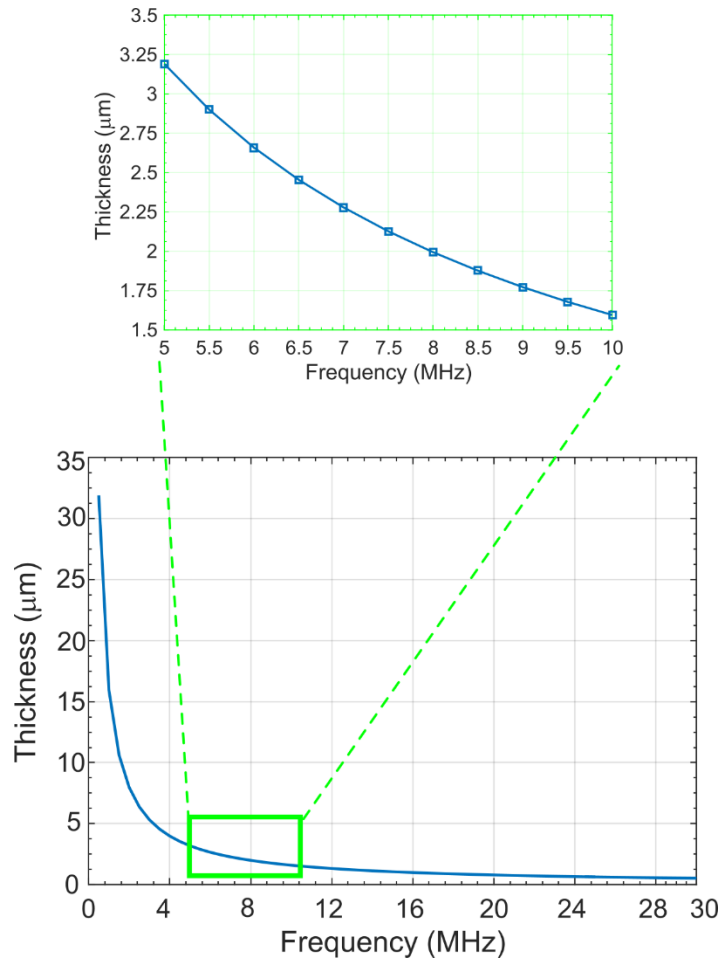
Figure 5-10. Coating thickness for various CMUT designs and frequency of interest.

CMUT designs and frequency of interest. For example, the curve shows a 1.8 µm coating of aerogel can effectively attenuate the interface wave at frequency 8 MHz. For the designed CMUT with center frequency 7.5 MHz, calculated aerogel thickness is 2.1µm. It can also be inferred from the plot that the lower thicknesses of the aerogel layer are necessary at higher frequencies. This frequency dependence can be related to attenuation of the Scholte wave. At frequencies below 12 MHz, the Scholte wave is nearly non-dispersive and travels without much reduction in wave energy. Thus, higher thicknesses (greater than 1 µm) of passivation layer are needed at frequencies below 12 MHz.

5.3.4 CMUT Arrays without Silica Aerogel Passivation Layer

In order to study the acoustic crosstalk effects in CMUT arrays, a 1D CMUT array consisting of five CMUT elements, each with five cells of sidelength 16 μm and thickness 1.3 μm along its width are modeled using FEA. The modeled array element and cells are shown in Figure 5-11. Due to the presence of symmetry in the CMUT array around the transmitter, only half of the array was modeled. A coupled acoustic-structure analysis is set up.
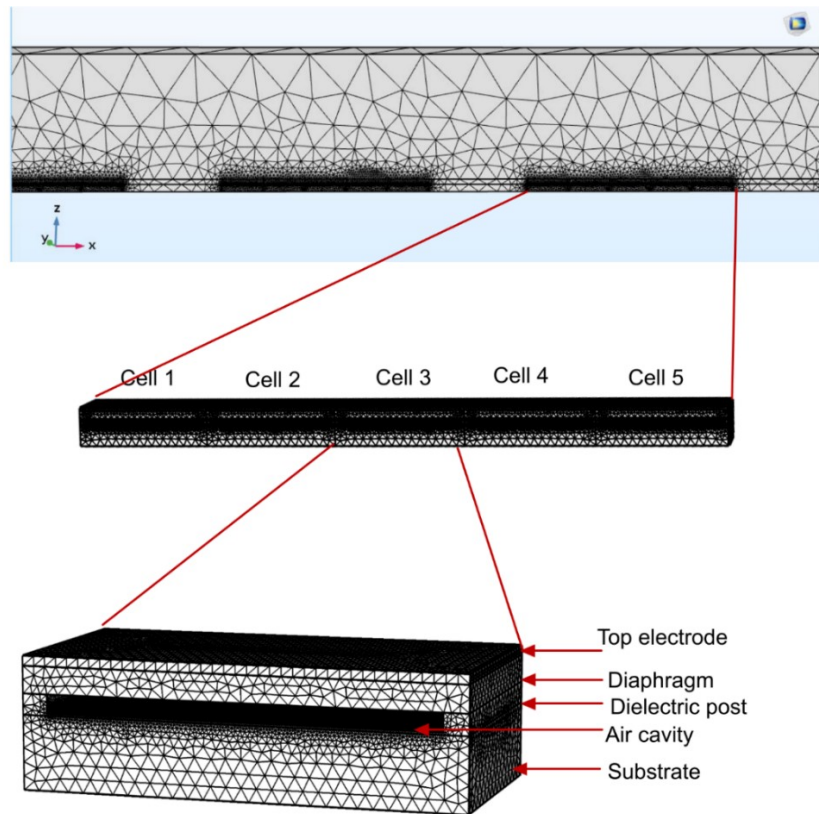

Figure 5-11. Simulation model for the CMUT array.

The physical dimensions and the material properties of the CMUT cell used in the FEA are as described in Table 5-3 and Table 5-4. The frequency response of the excited CMUT element is plotted in Figure 5-12 and spurious effects are observed

at around 7.5 MHz. Further analysis is carried out to calculate the level of crosstalk. This is done by exciting the center element in the water domain at a step frequency of 1 MHz throughout the -6 dB bandwidth i.e. 4 to 16 MHz. The normalized displacement frequency response of the nearest-neighbor and next-nearest elements are obtained to determine the relative level of crosstalk signal with respect to the excited element. The peak and the average crosstalk levels can be calculated through the analysis of the displacement frequency spectra of the neighboring inactive elements.

Table 5-3. Design specifications of the CMUT cell.

Parameter	Unit	Value
Cell sidelength, $L = 2a$	μm	16
Diaphragm thickness, d_m	μm	1.3
Airgap height, d_o	nm	650
Insulating layer thickness, d_i	nm	100
Top electrode thickness, t	nm	100
Contact pad thickness, t_c	μm	0.4
Dielectric post thickness, L_c	μm	2

Table 5-4. Material properties of the CMUT cell.

Parameter	Unit	BCB (Diaphragm)	Gold (Top electrode)	Silicon <100> (Substrate)
Density, ρ	kg/m^3	1050	19300	2329
Young's modulus, E	GPa	2.9	70	165
Poisson's ratio, v		0.34	0.44	0.26
Residual stress, σ	MPa	28	106	55
Relative permittivity, ε		2.6	6.9	11.8

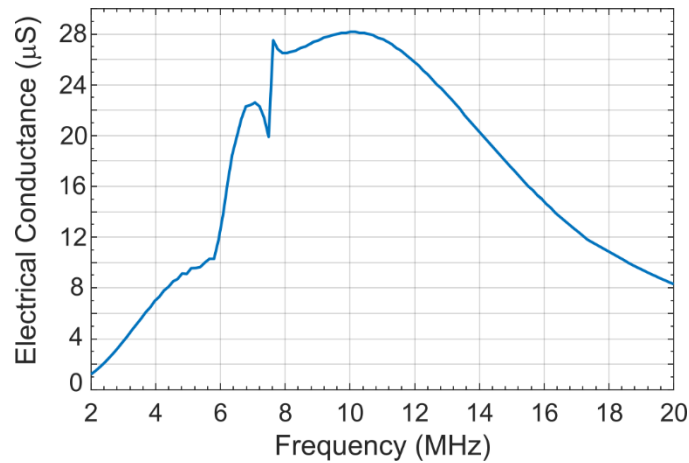Figure 5-12. Frequency Response of CMUT array element without aerogel coating.

As seen in Figure 5-13 and Table 5-5, the peak crosstalk level is -17.18 dB across the first neighbor. And, the average crosstalk level over the –6 dB bandwidth was calculated to be -22.44 dB with a standard deviation of 1.88 dB. The crosstalk level across the second neighbor was also calculated for comparison purposes.
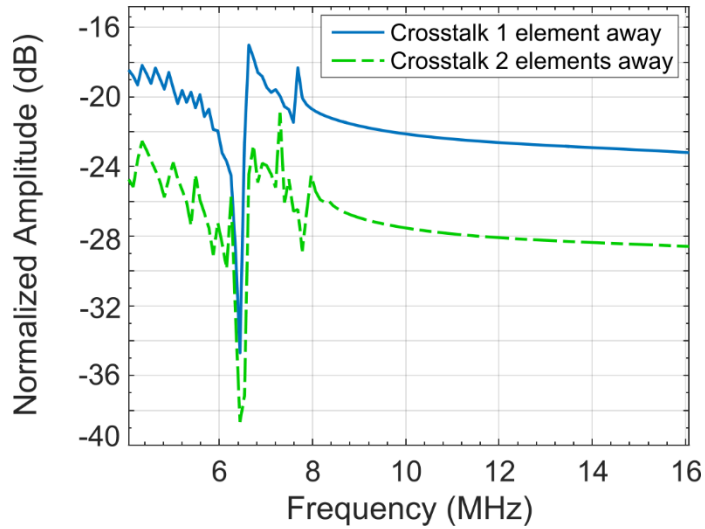
Figure 5-13. Crosstalk level at the nearest and the next neighbor without aerogel coating.

The peak crosstalk level was -21.07 dB as shown in Figure 5-13. The average crosstalk was calculated to be -27.46 dB. The level of crosstalk decreased linearly with the distance from the excited element. The simulated average CMUT element crosstalk levels were found to be consistent with the other published CMUT crosstalk level results elsewhere [8] which validated the correctness of the executed finite element methods.

Table 5-5. Peak and average crosstalk levels of the designed CMUT array without aerogel coating.

Element number	Peak Crosstalk Level (dB)	Average Crosstalk Level (dB)
1st neighbor	-17.18	-22.44
2nd neighbor	-21.07	-27.46

5.3.5 CMUT Arrays with Silica Aerogel Passivation Layer

A 2 μm thick aerogel layer is deposited on the CMUT array and the frequency response of the excited CMUT element was investigated. Although the frequency response still shows some crosstalk effects, the crosstalk effects in the

frequency region of interest i.e. between 6 to 10 MHz has fairly reduced. The corresponding frequency response for the excited element had a center frequency of 7.5 MHz with 114% fractional bandwidth as shown in Figure 5-14. The normalized displacement as a function of frequency for the nearest and the next nearest element are plotted. Compared to the case without the passivation layer, it was found that the crosstalk levels with the aerogel coating was slightly reduced. The crosstalk level curve for the first neighboring element showed a peak value of approximately -22.6 dB (Figure 5-15). The average level over the -6 dB fractional bandwidth was -27.4 dB compared to -22.44 dB for CMUT element without aerogel passivation layer coating.
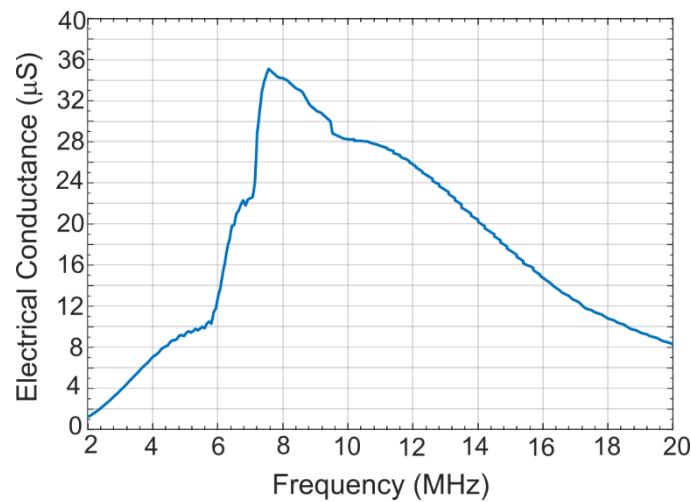

Figure 5-14 . Frequency Response of CMUT array element without aerogel coating.
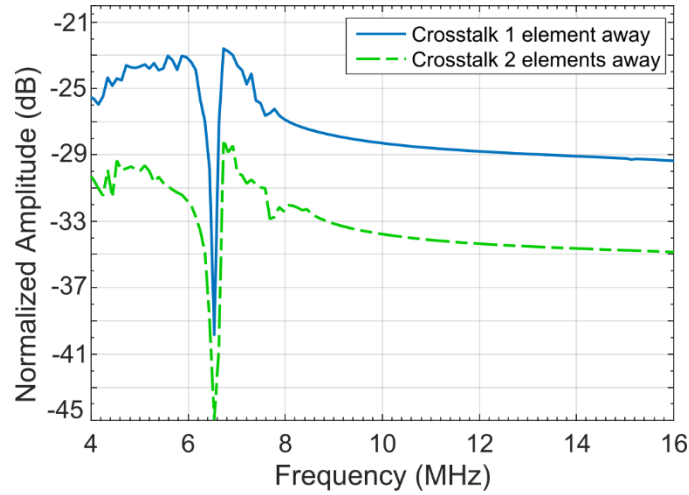
Figure 5-15. Crosstalk level at the nearest and the next neighbor with aerogel coating.

An average crosstalk level reduction of approximately 5 dB was achieved using the developed technique. Across the next nearest neighbor, the peak crosstalk level was -28.6 dB as shown in Figure 5-15 and Table 5-6. The average crosstalk was calculated to be -33.8 dB which was 6.34 dB lower than that without the aerogel layer.

Table 5-6. Peak and average crosstalk levels of the designed CMUT array with aerogel coating.

Element number	Peak Crosstalk Level (dB)	Average Crosstalk Level (dB)
1st neighbor	-22.6	-27.4
2nd neighbor	-28.6	-33.8

Thus, a reduction of about 5 dB in the average crosstalk level across the nearest neighboring element is observed with the addition of 2 μm silica aerogel coating for a 7.5 MHz CMUT array.

5.4   Discussions

Crosslinked silica-x-aerogels exhibit good thermal, electrical insulating properties, have the lowest sound speeds and preserve the static and the dynamic behavior of the CMUT that make them ideal passivation materials for CMUT arrays.

A FEM was developed to study the behavior of silica-aerogel protected CMUTs. The model was able to accurately simulate the correct static and dynamic responses of the CMUT element which validated the developed FEA. The acoustic crosstalk behavior between the CMUT elements was simulated and it was demonstrated that the aerogel passivation layer was able to effectively suppress the acoustic crosstalk level by at least 5 dB or more in comparison to CMUTs without the aerogel coating.

It was further seen that that the protective aerogel layer could be employed as crosstalk suppressants at other frequencies as well. Three CMUT array designs with center frequencies 3 MHz, 5 MHz and 30 MHz respectively were designed and the thickness of the coating was chosen based on Figure 5-10. Average crosstalk level reductions of approximately 4 dB to 5 dB were observed in each of the cases confirming the effectiveness of the aerogel layer at most frequencies. Table 5-7 presents a comparison of the crosstalk levels of the proposed CMUT array with the experimental results of a comparable CMUT array with PDMS coating, reported in [8].

Table 5-7. Validation of the design effectiveness.

Parameter	Presented design		Bayram et al. [8]	
Type	Conventional CMUT (simulated)	CMUT with aerogel passivation layer (simulated)	Conventional CMUT (experimental)	CMUT with PDMS passivation layer (experimental)
Diaphragm material	BCB	BCB	Silicon Nitride	Silicon Nitride
Center frequency (MHz)	7.5	7.5	5.8	5.8
Pitch (μm)	200	200	250	250
Number of elements	64	64	64	64
-6 dB Fractional bandwidth	133	114	130	100
Peak crosstalk level (dB)	-17.18	-22.6	-17	-17
Average crosstalk level (dB)	-22.44	-27.4	-23.2	-23.3

The comparison establishes that the presented design with the aerogel passivation layer is capable of providing approximately 5 dB reduction in the average crosstalk level in comparison with the 5 μm PDMS layer coating which showed no significant improvement.

Further, the average crosstalk levels of the designed CMUT array is compared with the crosstalk levels for the piezoelectric transducers [48][49][50]. For piezoelectrical transducers with center frequencies between 1 MHz to 10 MHz,

Table 5-8. Comparison of crosstalk levels between piezoelectric transducers and the designed CMUT.

Element No.	Average Crosstalk Level (dB)		
Transducer Type	Designed CMUT without aerogel (7.5 MHz)	Designed CMUT with aerogel (7.5 MHz)	PZT (1-10 MHz) [47]
1st neighbor	-22.44	-27.4	-30
2nd neighbor	-27.46	-33.8	-38

the average crosstalk level over the −6 dB array bandwidth is about −30 dB across the nearest element [48] and −38 dB across the next-nearest element [48]. Although the crosstalk levels of the designed CMUT array is still higher than that of the piezoelectric transducer, the developed technique with aerogel passivation layer shows considerable reduction and can be regarded as a technique that holds potential for the minimization of mutual acoustic crosstalk in CMUT arrays.

CHAPTER 6

FABRICATION OF THE PROPOSED CMUT ARRAY

This chapter presents the process flow sequence to fabricate the proposed CMUT array with top thin film lossy aerogel passivation layer. The details of each fabrication step are provided with operating conditions, materials used, process type and a conceptual cross-sectional view. Initial fabrication techniques involving the development of the BCB diaphragms have been used previously in our lab and detailed description of the process steps can be found in [17].

6.1   Fabrication Steps

STEP 1: Wafer Cleaning and Oxide Layer Deposition

A 500 μm thick <100> oriented silicon wafer (Wafer A) is selected as the substrate and is cleaned using standard RCA cleaning processes. Then,1 μm thick oxide passivation layer is grown on the wafer using thermal oxidation process as shown in Fig. 6.1.
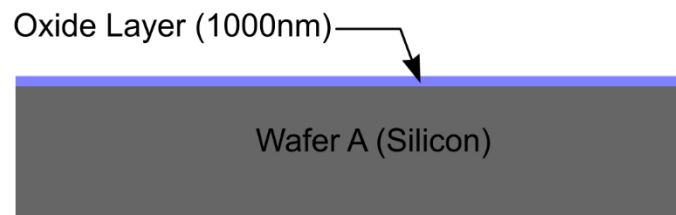

Figure 6-1. Thermal oxide passivation on wafer A.

STEP 2: Deposition of Top Metal Electrode

The second step includes deposition of the Gold layer, which forms the top electrode of the CMUT array, as shown in Figure 6.2. Since, gold doesn't adhere

well to oxide, a 30nm layer of titanium is deposited as a promoter. Following this step, a 200 nm thick Au layer is evaporated on the top of the titanium layer using electron beam evaporation process.
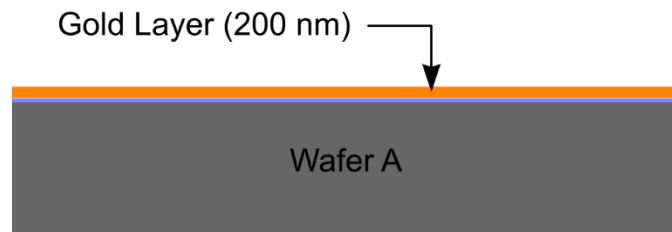
Gold Layer (200 nm) ——

Wafer A

Figure 6-2. Top metal electrode deposition.

STEP 3: Formation of BCB Membrane

Plasma cleaning is done on the wafer using highly reactive oxygen radicals to remove any organic contaminants and it is then vacuum baked at 150°C. A BCB adhesion promoter AP3000 [51] is then spin coated on top of the gold layer and the wafer is soft baked at 170°C for 2 minutes. This is followed by spin coating of 1.3 μm thick BCB (Cyclotene 3022-35) at a spin speed of 2300 rpm for 45 seconds and spread speed of 500 rpm for 5 seconds and partially curing of the BCB layer to achieve required stability [51].

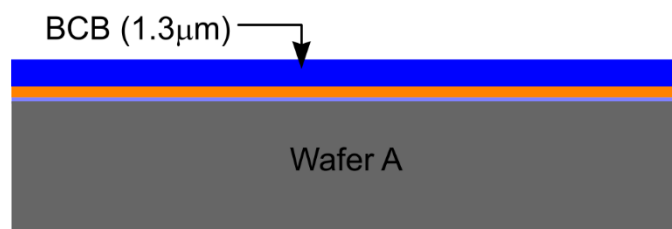BCB (1.3μm) ——

Wafer A

Figure 6-3. BCB layer deposition for CMUT membrane.

STEP 4: Deposition of BCB as an insulation layer and dielectric post

Another <100> oriented n-doped low resistivity silicon wafer (Wafer B) is RCA cleaned and a 1 μm thick oxide passivation layer is deposited on the wafer using thermal oxidation process. An 800 nm thick layer of BCB is then spin deposited and partially cured using techniques presented in step 3. The BCB layer is carefully RIE etched using a Bosch process for 4 minutes using 22.5 sccm of CF_4, 90 sccm of O_2 at 200 W RF power and 50 mTorr chamber pressure to form 650 nm CMUT cavities and the residual BCB thickness serves as an insulation layer. (Fig.6.4)
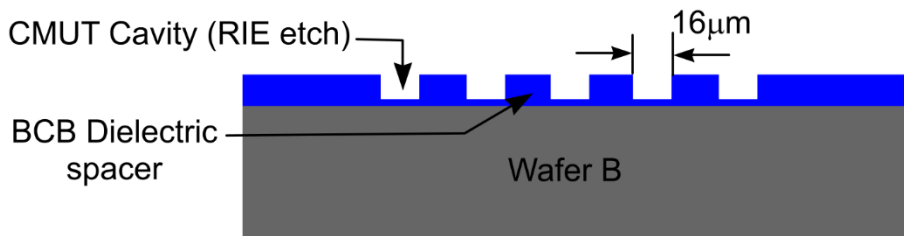

Figure 6-4. RIE etch of BCB layer to form CMUT air cavities.

STEP 5: Adhesive Bonding of Wafer A and Wafer B

Both wafers A and B are spin rinsed in di-ionized water and dried. Wafer A is then flipped and bonded with wafer B in vacuum (~10mTorr) using a thermal and pressure cycling processes. During bonding, the temperature is gradually increased to 150°C and the maximum bonding pressure is brought to 850 psi over a span of thirty minutes [17]. The wafers are then cured at 230°C for an hour.
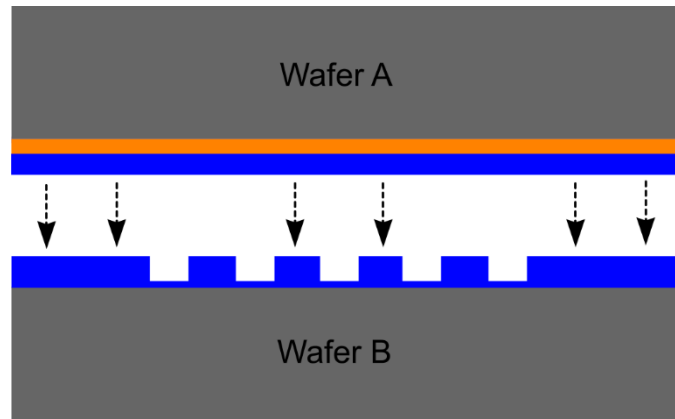
78

Figure 6-5. Adhesive wafer bonding of wafer A and wafer B.

STEP 6: Wet Etching of Silicon Layer

After bonding, the top silicon wafer in the stack is dissolved using a 25% hot KOH wet etch recipe at 100°C. The etching process is halted when it reaches the oxide layer and is cooled and cleaned. The oxide layer acts as a capping layer for aerogel layer deposition.
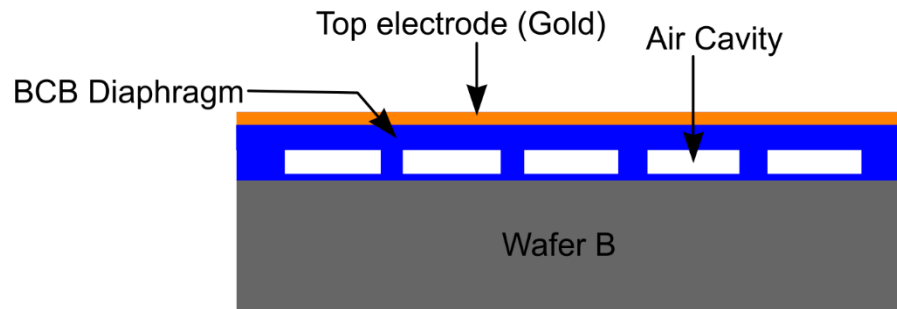

Figure 6-6. Dissolution of top wafer A.

The substrate is treated prior to thin film deposition. The CMUT sample is oxidized by UV Ozonation for 10 minutes, treated in 2 vol % cleaning solution for 30 minutes, rinsed with de-ionized (DI) water, blown dry with air, and treated again with UV Ozonation for 8 minutes. The UV-ozone-cleaning procedure is a highly

effective method to remove a variety of contaminants from surfaces. It is a simple-to use dry process which is inexpensive to set up and operate [33].

STEP 7: Silica Aerogel Sol Preparation

The silica sols are prepared from a sodium silicate (water glass) solution. Sodium silicate is mixed with distilled water in right proportions based on the porosity and pH requirements for the derived sol (For example, to prepare a sol of pH 2.4 with silica content 5.4 weight percent, 144ml of sodium silicate is mixed with 525ml of Di-ionized water in [52]). The diluted solution of sodium silicate is then passed through a column filled with an ion exchange resin (Amberlite). During this process, the trapping of Na^+ occurs along with simultaneous release of H^+ ions (ion exchange) by passing through an insoluble polymer matrix and silicic acid solution is formed [52]. A base catalyst (NH_4OH) can be added to create silica sols with higher pH values of 3.5 or 4.0 and initiate gelation. And, the mixture then begins to partially neutralize and condenses to form a sol.
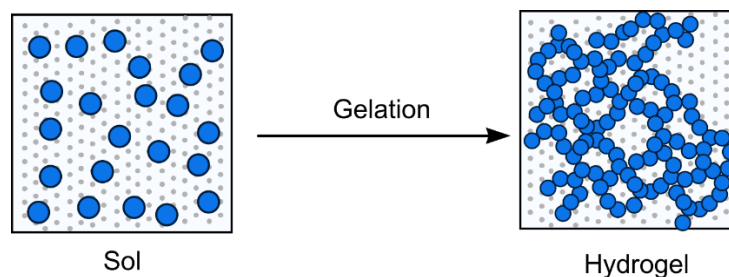

Figure 6-7. Formation of hydrogel [54].

STEP 8: Aging, Solvent Exchange and Surface Modification of the Gel

The formed hydrogel is aged at 50°C for 48 hours, followed by pore fluid-exchange of 100% ethanol, ethanol/hexane (3:1 v/v), ethanol/hexane (1:1 v/v), ethanol/hexane (1:3 v/v), and 100% hexane, respectively. These gels are then surface modified with APTES (aminopropyltriethoxysilane) (~25% v/v) in hexane at 60°C for 12 hours [53]. Surface functionalization of the alcogels facilitates ambient pressure drying process by reducing the capillary tension through the chemical modification of the hydrophilic gel surface [33]. It improves the mechanical strength of the aerogel and makes its surface, hydrophobic.
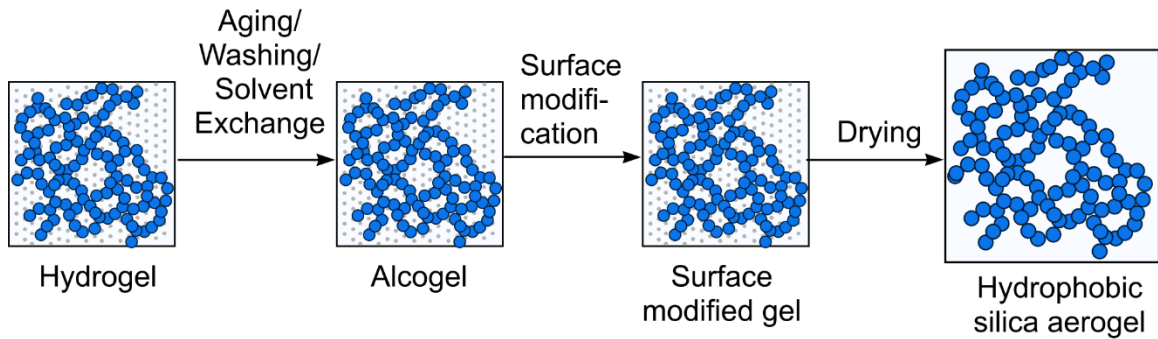

Figure 6-8. illustration of synthesis processes for silica aerogel production. Adapted with permission from [54].

STEP 9: Deposition of Top Thin Film Aerogel Layer

The aerogel is sonicated with ultrasound for about an hour until it becomes resoluble. An indirect synthesis methodology is employed where the aerogels are initially prepared indirectly prior to thin film deposition and during the time of sol-gel deposition, the functionalized gels are partially re-liquified using sonification by ultrasound and then spin coated onto wafers [33]. This type of indirect synthesis reduces solvent waste than the direct synthesis of films on the sample [33].

Additionally, it prevents the CMUT sample from unnecessary exposure. Since the aerogel have been subject to solvent exchange and surface modification processes, the drying process becomes revertible allowing the porosity of the film to expand, or spring back to its wet size.

Once the surface modified gels are re-liquified using ultrasound, they are then spin-coated onto oxide layer of the CMUT wafer at a speed of 2000 rpm for 15 seconds. The coated films are then ambient pressure dried in hexane at room temperature for 12 hours.
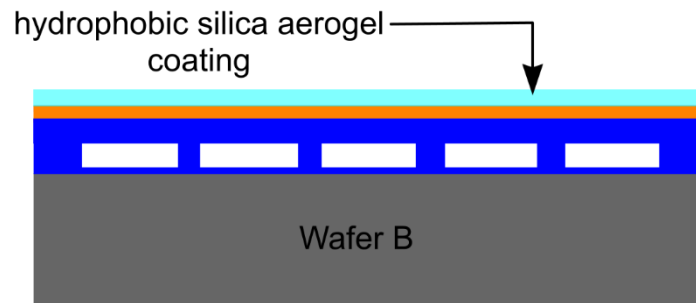

Figure 6-9.Thin film silica aerogel deposition.

STEP 10: Deposition of Gold Contact Pads

This step involves patterning the aerogel layer and then selectively etching of aerogel and oxide layer to expose the gold contact pad region using lift-off process. The lift off process begins with soft baking at 150°C, followed by spin coating of 3 μm of lift off resist LOR 30B. The photoresist AZ 9260 is then spin coated with spread speed of 500 rpm for 5 minutes and spin speed 3000 rpm for 45 minutes [51] and baking at 110°C for 3 minutes. The sample is then exposed to UV light at an exposure dose of 1100mJ/cm^2 [17]. The 2.1 μm thick aerogel

layer and oxide layer are carefully etched using plasma etching for 2 minutes. A 10 nm titanium is evaporated for better adhesion, followed by 500 nm of gold using electron-beam evaporation. AZ-400K developer is used to complete the lift off process. Any trapped photoresist in the nanopores of the aerogel thin films during photoresist coating is removed through O_2 Plasma cleaning.
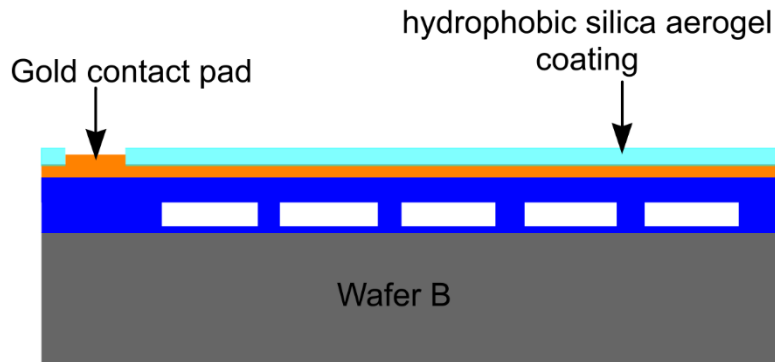
Figure 6-10. Deposition of gold contact pads.

Thus, a hydrophobic thin film silica aerogel with improved strength can be fabricated on BCB based CMUT diaphragms using these cost-efficient waterglass sol-gel and ambient pressure drying processes. Solvent to solute ratios determine the aerogel's porosity and the reaction time and acid–base catalysts largely impact to the pore size. This simple yet effective modification to the CMUT design, makes aerogels suitable as top passivation layers for CMUTs with reduced mutual crosstalk.

CHAPTER 7

CONCLUSIONS

7.1 Conclusions

In this research work, a novel technique involving Di-isocyanate enhanced crosslinked silica aerogel as passivation layer on the CMUT top surface for crosstalk reduction due to Scholte waves is adopted. 3D finite element analysis carried out using COMSOL Multiphysics showed that the developed technique can reduce the crosstalk by at least 5 dB more at the nearest neighbor as compared to other techniques published elsewhere [8]. An added advantage of the developed technique is that the level of Scholte wave attenuation can be controlled by altering the porosity of the aerogel layer.

Investigations were carried out on several CMUT test geometries to identify the causes of crosstalk before the optimization process. The crosstalk due to Scholte waves is identified as the major issue which affects the frequency response of the CMUT leading to inaccuracies during image reconstruction. The magnitude of crosstalk in the frequency response is found to dependent on the intensity of Scholte waves at any particular cell diaphragm, which is influenced by diaphragm sidelength, fill factor, the fluid coupling medium and the number of cells in the CMUT element.

A fabrication process involving typical MEMS sol-gel is proposed for the aerogel passivation layer deposition. The waterglass method involving aqueous solution of sodium silicate in ion-exchange resin is used for the sol preparation.

During the ageing and the purifying process of the aerogel, its surface is modified by crosslinking with Di-isocyanate agent to make it hydrophobic and improve its mechanical strength. The hydrophobic silica aerogel is insensitive to moisture content in the atmosphere and can resist the capillary forces exerted by the environment. As a result, ambient drying techniques can be employed to fabricate the aerogel instead of super-critical drying processes. This accounts for a relatively easy and cost-effective method of aerogel passivation layer deposition, which does not interfere with the conventional CMUT's fabrication process flow.

The developed technique involving crosslinked silica aerogel shows promise of mitigating acoustic crosstalk in CMUT array elements due to Scholte waves. This technique will serve to be beneficial in improving the signal to noise ratio and the imaging quality of the CMUT array and will aid the potential deployment of CMUT for NDE application.

7.2   Future Directions

The developed technique is validated using analytical model designed in MATLAB and through comparison with the experimental results of comparable CMUT arrays published elsewhere [8]. Fabrication and experimental characterization of the CMUT array with crosslinked silica aerogel passivation layer is in progress and will further add value to the proposed technique.

Improvements can be made to pursue further understanding of the crosstalk patterns for optimization by investigating the effect of residual stress of the diaphragm material and the dielectric spacers on the CMUT's frequency response.

Additionally, a design strategy based on the removal of a few center membranes, followed by average and interpolation to compensate for any loss of acoustic output can also be explored as a possible technique to mitigate the distortions in the frequency response of a CMUT element in an array and minimize the crosstalk effects further.

This research work is focused towards reduction of acoustic crosstalk effects due to Scholte waves at the fluid-CMUT interface. Investigation is also necessary to explore techniques to reduce the acoustic crosstalk effects in the CMUT array due to propagation and mode conversion of the Lamb waves in the thin silicon substrate and the crosstalk effects due to capacitive coupling between the individual CMUT array elements.

Acoustic lens formed on the CMUT to mechanically focus ultrasound is usually made of silicone rubber for acoustic impedance matching and encapsulation. It is interesting to investigate the possible use of flexible and mechanically strong silica aerogels in place silicone rubber in the ultrasound probe as lenses for beam focusing in air coupled CMUT lens. The aerogel materials hold promises of improving the CMUT's overall performance and future research work focused in this direction is needed to fully exploit their capabilities.

REFERENCES/BIBLIOGRAPHY

[1]   "Global Non-Destructive Testing Equipment Market Worth $2200 Million by 2018," *NDT.net Journal*, 2016. [Online]. Available: http://www.ndt.net/search/docs.php3?id=13895&content=1.

[2]   X. Zhuang, "Capacitive Micromachined Ultrasonic Transducers with Through Wafer Interconnects," PhD Dissertation , Stanford University, 2008.

[3]   L. L. P. Wong, "Capacitive Micromachined Ultrasonic Transducers for Non-destructive Testing Applications," PhD Dissertation, University of Waterloo, Canada, 2014.

[4]   M. Hochman, "Investigation of acoustic crosstalk effects in CMUT arrays," Master's Thesis , Dept. of Mechanical Engineering, Georgia Institute of Technology.

[5]   B. Bayram, G. G. Yaralioglu, M. Kupnik, a. S. Ergun, O. Oralkan, a. Nikoozadeh, and B. T. Khuri-Yakub, "Dynamic analysis of capacitive micromachined ultrasonic transducers," *IEEE Trans. Ultrason. Ferroelectr. Freq. Control*, vol. 52, no. 12, pp. 2270–2275, 2005.

[6]   B. Bayram and B. Khuri-Yakub, "Acoustic Crosstalk Reduction for Capacitive Micromachined Ultrasonic Transducers in Immersion," US 20080259725AI, 2008.

[7]   E. Campbell, L. A. J. Davis, G. Hayward, and D. Hutchins, "Cross-coupling in sealed cMUT arrays for immersion applications," *Proc. - IEEE Ultrason.*

Symp., pp. 2135–2138, 2007.

[8]   B. Bayram, M. Kupnik, G. G. Yaralioglu, Ö. Oralkan, A. S. Ergun, D. S. Lin, S. H. Wong, and B. T. Khuri-Yakub, "Finite element modeling and experimental characterization of crosstalk in 1-D CMUT arrays," *IEEE Trans. Ultrason. Ferroelectr. Freq. Control*, vol. 54, no. 2, pp. 418–429, 2007.

[9]   D. S. Lin, "Interface Engineering of Capacitive Micromachined Ultrasonic Transducers for Medical Applications," PhD Dissertation , Stanford University, 2011.

[10]   S. Berg, "Capacitive micromachined ultrasonic transducers - Acoustic challenges and proposed solutions," PhD Dissertation, Dept. of Electronics and Telecommunications, Norwegian University of Science and Technology, Trondheim, 2012.

[11]   S. Zhou and J. A. Hossack, "Reducing inter-element acoustic crosstalk in capacitive micromachined ultrasound transducers," *IEEE Trans. Ultrason. Ferroelectr. Freq. Control*, vol. 54, no. 6, pp. 1217–1228, 2007.

[12]   Wikipedia, "Non-destructive Testing." [Online]. Available: https://en.wikipedia.org/wiki/Nondestructive_testing.

[13]   A. Barbian, M. Beller, S. Hartmann, and U. Schneider, "High Resolution Ultrasonic In-Line Inspection: Added Value and Special Applications," *6th Pipleine Technol. Conf.*, 2011.

[14]   Integrated Sensing Systems Inc., "Technology : Capacitive Sensing."

[Online]. Available: https://mems-iss.com/mems-technologies/.

[15] W. . Eaton and J. . Smith, "Micromachined pressure sensors : review and recent developments," *J. Smart Mater. Struct.*, vol. 6, pp. 530–539, 1997.

[16] M. Meloche and S. Chowdhury, "Design of a MEMS discretized hyperbolic paraboloid geometry ultrasonic sensor microarray," *IEEE Trans. Ultrason. Ferroelectr. Freq. Control*, vol. 55, no. 6, pp. 1363–1372, 2008.

[17] R. Manwar, "A BCB Diaphragm Based Adhesive Wafer Bonded CMUT Probe for Biomedical Application," PhD Dissertation, Dept. of Electrical and Computer Engineering, University of Windsor , Canada, 2017.

[18] T. Zure, "Characterization of a CMUT Array," Master's thesis, Dept. of Electrical and Computer Engineering, University of Windsor , Canada, 2012.

[19] V. Yashvanth and S. Chowdhury, "A New Scheme for High Frequency Ultrasound Generation," in *2017 IEEE 30th Canadian Conference on Electrical and Computer Engineering (CCECE)*, 2017, pp. 350–353.

[20] J. B. U. Haldorsen, D. L. Johnson, T. Plona, B. Sinha, H.-P. Valero, and K. Winkler, "Borehole Acoustic Waves," *Oilf. Rev. Spring*, vol. 18, no. 1, pp. 34–43, 2006, ©Schlumberger.

[21] Z. Nazarchuk, V. Skalskyi, and O. Serhiyenko, "Propogation of Elastic Waves in Solids" in Acoustic Emissions : Methodology and Application. ©Springer International Publishing AG 2017.

[22] X. Jin, Ö. Oralkan, F. L. Degertekin, and B. T. Khuri-Yakub,

"Characterization of one-dimensional capacitive micromachined ultrasonic immersion transducer arrays," *IEEE Trans. Ultrason. Ferroelectr. Freq. Control*, vol. 48, no. 3, pp. 750–760, 2001.

[23] Ö. Oralkan, A. S. Ergun, J. A. Johnson, M. Karaman, U. Demirci, K. Kaviani, T. H. Lee, and B. T. Khuri-Yakub, "Capacitive micromachined ultrasonic transducers: Next-generation arrays for acoustic imaging?," *IEEE Trans. Ultrason. Ferroelectr. Freq. Control*, vol. 49, no. 11, pp. 1596–1610, 2002.

[24] K. Chapagain, "Integration of Electronics and Mechanics in Next Generation Ultrasound Transducers in Medical Imaging," PhD Dissertation, Dept. of Electronics and Telecommunication ,Norwegiam University of Science and Technology, 2014.

[25] F. Pavlo, "Capacitive micromachined ultrasonic transducer (cMUT) for biometric applications," Master's Thesis, Dept. of Nanoscience and Technology, Chalmers University of Technology, Sweden, 2012.

[26] R. Zhang, C. Xue, C. He, Y. Zhang, J. Song, and W. Zhang, "Design and performance analysis of capacitive micromachined ultrasonic transducer (CMUT) array for underwater imaging," *Microsyst. Technol.*, vol. 22, no. 12, pp. 2939–2947, 2016.

[27] M. Rahman, J. Hernandez, and S. Chowdhury, "An improved analytical method to design CMUTs with square diaphragms," *IEEE Trans. Ultrason. Ferroelectr. Freq. Control*, vol. 60, no. 4, pp. 834–845, 2013.

[28] D. Maier-Schneider, J. Maibach, and E. Obermeier, "A new analytical solution for the load-deflection of square membranes," *J. Microelectromechanical Syst.*, vol. 4, no. 4, pp. 238–241, 1995.

[29] "Materials Advances; Namics, Towa, Dow;," *IFTLE 173 IMAPS 2013 –3D Integration Handbook, Wiley VCH*, 2013. [Online]. Available: http://electroiq.com/insights-from-leading-edge/2013/12/iftle-173-imaps-2013-materials-advances-namics-towa-dow-wiley-vch-reading-vol-3/.

[30] B. Merle and M. Göken, "Fracture toughness of silicon nitride thin films of different thicknesses as measured by bulge tests," *Acta Mater.*, vol. 59, no. 4, pp. 1772–1779, 2011.

[31] J. Cross, R. Goswin, R. Gerlach, J. Fricke, J. Cross, R. Goswin, R. Gerlach, J. F. Mechanical, P. Of, and S. Aerogels, "Mechanical Properties of SiO2 Aerogels," vol. 50, 1989.

[32] J. Gross, G. Reichenauer, and J. Fricke, "Mechanical properties of SiO 2 aerogels," *J. Phys. D. Appl. Phys.*, vol. 21, no. 9, pp. 1447–1451, 1988.

[33] E. Yang, "Fabrication and Preliminary Characterization of Hydrophobic Silica Aerogel Films for Oil Remediation Studies," Pomona Senior Theses, Paper 97, 2011.

[34] S. B. Riffat and G. Qiu, "A review of state-of-the-art aerogel applications in buildings," *Int. J. Low-Carbon Technol.*, vol. 8, no. 1, pp. 1–6, 2013.

[35] G. Carlson, D. Lewis, K. McKinley, J. Richardson, and T. Tillotson, "Aerogel

commercialization: technology, markets and costs," *J. Non. Cryst. Solids*, vol. 186, pp. 372–379, 1995.

[36] Springer Nature, "Aerogels Handbook," M. A. Aegerter, N. Leventis, M. M. Koebel ,Edition 1, pp. 21–46, 2011, **DOI** 10.1007/978-1-4419-7589-8

[37] I. Smirnova, T. U. H.- Harburg, and T. Verfahrenstechnik, "Applications of aerogels in life sciences."

[38] A. Du, B. Zhou, Z. Zhang, and J. Shen, "A special material or a new state of matter: A review and reconsideration of the aerogel," *Materials (Basel).*, vol. 6, no. 3, pp. 941–968, 2013.

[39] "Aerogels." [Online]. Available: http://www.aerogel.org.

[40] S. M. Attia, M. S. Abdelfatah, and M. M. Mossad, "Conduction mechanism and dielectric properties of pure and composite resorcinol formaldehyde aerogels doped with silver," *J. Phys. Conf. Ser.*, vol. 869, no. 1, 2017.

[41] L. Foresta, V. Gibiata, and W. T, "Biot's theory of acoustic propogation in porous media applied to aerogels and alcogels," *J. Non. Cryst. Solids*, vol. 225, pp. 287–292, 1998.

[42] M. Aegerter, N. Leventis, and M. Koebel, *Aerogels handbook (Advances in Sol-Gel Derived Materials and Technologies)*. 2011.

[43] J. Conroy, B. Hosticka, S. . Davis, and P. Norris, "Evaluation of the Acoustic Properties of Silica Aerogel," in *Symposium, Porous,cellular and microcellular materials, ASME-Publications* , 1998, pp. 25–34.

92

[44]   M. Gronauer and J. Fricke, "Acoustic Properties of Microporous SiO2 aerogel," *Acustica*, vol. 59, no. 3, pp. 177–181, 1986.

[45]   Maynard, "Elastic and thermal properties of hierarchical structures :Application to silica aerogel," *Elsevier*, vol. 157, no. 1, pp. 601–609, 1989.

[46]   J. Lei, J. Hu, and Z. Liu, "Mechanical Properties of Silica Aerogel - A Molecular Dynamics Study," *2013 World Congr. Adv. Struct. Eng. Mech.*, pp. 778–785, 2013.

[47]   J. S. R. Murillo, M. E. Bachlechner, F. A. Campo, and E. J. Barbero, "Structure and mechanical properties of silica aerogels and xerogels modeled by molecular dynamics simulation," *J. Non. Cryst. Solids*, vol. 356, no. 25–27, pp. 1325–1331, 2010.

[48]   I. Bonded, M. Jonathan, J. Williams, and K. Kirk, "A High-Frequency Linear Ultrasonic Array," *Development*, vol. 58, no. 10, pp. 2202–2212, 2011.

[49]   H. C. Yang, J. Cannata, J. Williams, and K. Shung, "Crosstalk Reduction for High-Frequency Linear Array Ultrasound Transducers Using 1-3 Piezocomposites with Pseudo-Random Pillars," *IEEE Trans Ultrason Ferroelectr Freq Control*, vol. 40, no. 6, pp. 1301–1315, 2012.

[50]   E. Light, J. Angle, and S. Smith, "Real-Time 3D Ultrasound Guidance of Interventional Devices," *IEEE Trans Ultrason Ferroelectr Freq Control*, vol. 292, no. 3, pp. 342–351, 2009.

[51] R.   Manwar   and   S.   Chowdhury,   "Experimental   Analysis   of Bisbenzocyclobutene   Bonded   Capacitive   Micromachined   Ultrasonic Transducers," *Sensors*, vol. 16, no. 7, p. 959, 2016.

[52] Y. C. Cha, C. E. Kim, S. Lee, H. J. Hwang, J. W. Moon, I. S. Han, and S. Woo, "Synthesis of Silica Aerogel Thin Film from Waterglass," vol. 126, pp. 671–674, 2007.

[53] M. A. B. Meador, E. F. Fabrizio, F. Ilhan, A. Dass, G. Zhang, P. Vassilaras, J. C. Johnston, and N. Leventis, "Cross-linking Amine-Modified Silica Aerogels with Epoxies : Mechanically Strong Lightweight Porous Materials," no. 2, pp. 1085–1098, 2005.

[54] Rao A.V., Pajonk G.M., Bangi U.K.H., Rao A.P., Koebel M.M, "Sodium Silicate Based Aerogels via Ambient Pressure Drying," In Aegerter M., Leventis N., Koebel M. - Aerogels Handbook. Advances in Sol-Gel Derived Materials and Technologies, Edition 1, Chapter 2, pp. 103–124, 2011, **DOI** 10.1007/978-1-4419-7589-8 , © Springer Nature, All Rights Reserved, 2011.

APPENDIX – COPYRIGHT PERMISSIONS

Licensed Content Publisher
Springer Nature
Licensed Content Publication
Springer eBook
Licensed Content Title
Sodium Silicate Based Aerogels via Ambient Pressure Drying
Licensed Content Author
A. Venkateswara Rao, G. M. Pajonk, Uzma K. H. Bangi et al
Licensed Content Date
Jan 1, 2011
Type of Use
Thesis/Dissertation
Requestor type
academic/university or research institute
Format
electronic
Portion
figures
Title
CMUT Crosstalk Reduction Using Crosslinked Silica Aerogel

Terms and Conditions

Dear Varshitha Yashvanth,

This letter concerns your request to use certain images and/or animations owned by Schlumberger referenced in Exhibit A (J. B. U. Haldorsen, D. L. Johnson, T. Plona, B. Sinha, H.-P. Valero, and K. Winkler, "Borehole Acoustic Waves," *Oilf. Rev. Spring*, ©Schlumberger. The images are referred to collectively as the "Images") in Master's Thesis titled "CMUT Crosstalk Reduction using Crosslinked Silica Aerogel" which will be uploaded on University of Windsor Thesis and Dissertation Collection (http://scholar.uwindsor.ca/etd/) for educational purposes (hereinafter the "Work").

Schlumberger hereby grant you a non-exclusive, non-transferable, limited license to use reasonable portions of the Images solely for inclusion in the Work. The foregoing license (the "License") is based on your agreement to adhere to the following conditions:

- Schlumberger retains ownership in and to the Images and any associated trademarks, and has no affiliation whatsoever with the author or the Work;

- You acknowledge in the Work that portions of the Images are used in the Work, and that the Images and any associated trademarks are owned by Schlumberger;

The License shall automatically terminate upon the expiration or termination of Schlumberger's rights in and to the Images. The License is granted specifically based upon Schlumberger's understanding that the Work will be as described in the request and is contingent on the request being - at all times - complete, correct, and made in good faith.

VITA AUCTORIS

NAME:	Varshitha Yashvanth
PLACE OF BIRTH:	Karnataka, India
YEAR OF BIRTH:	1990
EDUCATION:	Bachelor of Engineering, Electronics and Communication Engineering, People Education Society Institute of Technology(PESIT), KA, India, 2012.
	Master of Applied Science in ECE, University of Windsor, Windsor, Ontario, Canada, 2018.